J Mater Sci (2025) 60:25386–25408

Energy materials

Engineering electron density and structural properties of CuO anode material via calcination and in situ synchrotron XRD for enhanced lithium-ion battery performance

W. T. R. S. Fernando[1], T. H. N. G. Amaraweera[1,2], K. M. D. C. Jayathilaka[3], L. S. R. Kumara[4], O. Seo[4], K. Osaka[4], O. Sakata[4], R. P. Wijesundera[3], and H. W. M. A. C. Wijayasinghe[1,*]

[1] *National Center for Advanced Battery Research, National Institute of Fundamental Studies, Kandy, Sri Lanka*
[2] *Department of Applied Earth Sciences, Uva Wellassa University, Badulla, Sri Lanka*
[3] *Department of Physics and Electronics, University of Kelaniya, Kelaniya, Sri Lanka*
[4] *Japan Synchrotron Radiation Research Institute (JASRI), Kouto, Sayo-Cho, Sayo-Gun, Hyogo 679-5198, Japan*

Received: 14 August 2025
Accepted: 26 October 2025
Published online: 19 November 2025

ABSTRACT

This research focused on engineering the electron density distribution and structural characteristics of CuO, including stacking fault probability, lattice strain, crystallite size, and dislocation density, through calcination to enhance the electrochemical performance of lithium-ion batteries (LIBs) when used as anode electrodes. The CuO material was synthesized by the simple and convenient chemically precipitated technique. Techniques such as laboratory X-ray diffraction (XRD), synchrotron X-ray diffraction (SXRD), Raman spectroscopy, and X-ray photoelectron spectroscopy (XPS) confirmed the formation of CuO. The electron density distribution and structural properties were analyzed via and XRD and SXRD Rietveld refinement. The results indicated that the optimal electrochemical performance was achieved with CuO calcined at 400 °C. In situ SXRD characterization of this CuO was performed to investigate its crystallographic parameters and stability over temperature range from − 100 to 600 °C. The crystal structure contracted and expanded for lower and higher temperatures, respectively, in comparison with room temperature. The CuO-400 anode exhibited better electrochemical performance, achieving a specific discharge capacity of 2751.7 mA h g^{-1} at a rate of 1.0 C, approximately a 50% improvement over the as-synthesized CuO anode. After 100 cycles, CuO-400 electrode at 400 °C delivered a specific discharge capacity of 364.2 mA h g^{-1} and a Coulombic efficiency of 98%. This enhanced electrochemical performance is

Handling Editor: Biao Chen.

Address correspondence to E-mail: athula.wi@nifs.ac.lk

https://doi.org/10.1007/s10853-025-11758-w

attributed to the optimized electron density distribution and structural properties of CuO, which improve its effectiveness as an anode material.

Introduction

Currently, lithium-ion batteries (LIBs) have become the advanced energy storage devices for portable electronic appliances, including electric vehicles (EVs) [1]. To date, graphite (both synthetic and natural) is considered the leading commercial anode material for LIBs [2, 3]. However, the graphite anode shows some limitations, such as a low theoretical capacity of 372 mA h g^{-1} [4]. Additionally, it requires detrimental process to produce battery grade graphite [5]. Therefore, the use of graphite anodes limits the development of LIBs.

In 2000, Tarascon et al. introduced transition metal oxides (TMOs)-based innovative anode materials to overcome the above-mentioned limitations of graphite anodes [6]. Lately, TMOs have gained considerable interest as anode materials due to their superior theoretical specific capacities compared to conventional graphite anode [6, 7]. Among these, CuO is recognized as a significant semiconductor with diverse applications, including solar cells [8], supercapacitors [9], catalysts [10], gas sensors [11], and LIBs [12]. Particularly, CuO is regarded as a promising anode material for LIBs because of its prominent advantages of a high theoretical capacity of 674 mA h g^{-1}, affordability, availability, safety, non-toxicity, high purity, environmental friendliness, ease of production, chemical stability, and storage convenience [4, 12, 13]. Li et al. reported an initial specific discharge capacity of 910 mA h g^{-1} at a current density of 50 mA g^{-1} [14]. In 2020, Wei et al. showed an initial specific discharge capacity of 609.5 mA h g^{-1} at a rate of 0.5 C [15]. In 2015, Zhang et al. demonstrated impressive electrochemical performance of a full cell of LIB using CuO as the anode and $LiNi_{0.5}Mn_{1.5}O_4$ as the cathode [16]. Additionally a full cell of LIB with CuO as the anode and $LiMn_2O_4$ as the cathode exhibited excellent electrochemical performance in 2020, as reported by Jose et al. [17]. All these previous literature intensify the potential of using CuO as an anode electrode for LIBs.

The synthesis process, including chemical precipitation, hydrothermal technique, is important for the structural properties of CuO. Ali et al. reported the structural and optical properties of CuO variation with different concentration of NaOH via chemical precipitation method [18]. Chauhan et al. have shown the depending on the structural and optical properties of CuO via the techniques such as microwave irradiation, co-precipitation, and hydrothermal [19]. Electrochemical performance of LIBs strongly depends on morphological interfacial properties of CuO/electrolyte and structural properties of CuO, including crystallographic parameter of CuO, electron density distribution, stacking fault probability, lattice strain, crystallite size, dislocation density, and CuO/Cu interfacial properties. To date, different morphological modifications have been investigated to enhance the CuO/electrolyte interfacial properties to boost electrochemical performance. Under that, different morphological modifications have been obtained by different synthesizing techniques. Octahedral CuO micro/nanocrystals [20], hierarchical nanostructured CuO [21], and three-dimensional clusters of peony-shaped CuO nanosheets [22] have been obtained via the chemical precipitate method. CuO microspheres [23], CuO nanoparticles [24], and sheaf-like CuO [25] have been reported by the hydrothermal method. In addition, calcination is a significant technique for obtaining morphologically modified CuO, such as CuO hierarchical structures [12] flower-like CuO [23], thorn-like CuO [23], and porous CuO nanoleaves [26]. Waser et al. reported CuO particles with diameters of 6–50 nm by spray pyrolysis to improve the electrochemical performance of LIBs [27]. In 2025, Fernando et al. have discussed the importance of CuO/Cu electronic interfacial via the optical properties and electrical properties for the electrochemical performance of CuO anode in addition to microstructured sponge-like morphology [28]. Electron density distribution, stacking fault probability, lattice strain, crystallite size, and dislocation density in electrode materials are critical characteristics for the conversion mechanism, and optimizing those properties for CuO anode materials for balancing ionic transport to enhance electrochemical performance. In 2012, Ren et al. studied the strain effect on the electrochemical properties of Li_2MnO_3 cathode material [29]. Stein et al. and his group studied the effect of crystallite

size of $LiNi_{1/3}Co_{1/3}Mn_{1/3}O_2$ cathode electrodes for LIBs in 2016. In 2018, Yue et al. investigated the optimum crystallite size for $Li_4Ti_5O_{12}$ anode electrodes [30]. Of the present study, the objective was to investigate the influence of crystallographic parameter of CuO, electron density distribution, stacking fault probability, lattice strain, crystallite size, dislocation density, and CuO/Cu interfacial properties on the electrochemical performance of CuO prepared by calcination at various temperatures of the particles initially synthesized by chemical precipitated technique. To the best of our knowledge, such an account of information relating to effect of structural properties for the electrochemical performance of LIBs has not been published before. In addition, the thermal stability of electrode material is a vital characteristic for the electrochemical performance of LIBs. Many authors have reported the importance of thermal stability of electrode material for the electrochemical performance of LIBs [31–33]. The existence of crystallographic phases in anode materials, which undergo a low-temperature to high-temperature variation, confirms the enhanced safety of LIBs. Hence, in situ synchrotron X-ray diffraction is performed on the optimum anode material to investigate its thermal stability under sudden changes in in situ temperatures from − 100 to 600 °C. As far as, we are aware, no previous studies have reported this type of investigation on CuO anode electrode material for LIB applications. Along with that, the present study was based on the synthesis of CuO by chemical precipitation, which is a simple, affordable, non-toxic, high-safety, and more environmentally benign method. The main objective of this study was to engineer the electron density, structural properties, and thermal stability of CuO anode material through calcination, aiming to achieve the best electrochemical performance in LIB applications.

Experimental details

Materials preparation

Analytically graded $Cu(NO_3)_2{\cdot}3H_2O$ (VWR) and NaOH (VWR) were utilized as the initial materials. Previous studies of this investigation show that CuO was synthesized via facile chemical precipitation technique for different concentrations of $Cu(NO_3)_2$ in a range from 0.001 to 0.1 M, the best electrochemical performance for sponge-like microstructured CuO that synthesized 0.03 M concentration of $Cu(NO_3)_2$ [28]. It was futher continued via calcination process to enhance the electrochemical performance. Analytically graded $Cu(NO_3)_2{\cdot}3H_2O$ (VWR) and NaOH (VWR) were utilized as the initial materials. First, 1.91 g of $Cu(NO_3)_2{\cdot}3H_2O$ was dissolved in 200 mL of deionized water while stirring magnetically at room temperature. Then, the solution was heated to 50 °C for 1 h with vigorous stirring. Pellet form of solid NaOH (0.05 g) was added gradually to the solution until a black precipitate formed. The mixture was kept at 50 °C for an additional 30 min. The black precipitated product was washed multiple times with deionized water to eliminate any residuals, continuing until the pH reached 7. The precipitate was then dried at 80 °C. Then, an initial calcination study was conducted to identify the optimum calcination temperature for achieving the best electrochemical performance. For this, the dried powder was separated into several batches, with each batch being calcined at different temperatures up to 600 °C. Separated powder batches were named as CuO-25 for as-synthesized CuO, CuO-200, CuO-400, and CuO-600 for the calcination temperatures of 200, 400, and 600 °C, respectively. Then the as-synthesized CuO and calcined CuO powder samples from each batch were subjected to the electrochemical performance analysis, through the procedure explained below under electrochemical characterization. It was found that the improved electrochemical performance was shown for the all calcined CuO, while showing notable electrochemical performances for the CuO-400, calcined at 400 °C for 2 h.

Material characterization

The phase analysis of the synthesized CuO samples were conducted using laboratory X-ray diffraction (XRD) with a Rigaku Ultima IV X-ray diffractometer, employing Cu Kα radiation (λ = 1.5406 Å) over a range of 10°–80°, at a scan rate of 1° s^{-1} and a step size of 0.20°. To gain deeper insights into the formation of Cu_xO phases during synthesis and the crystallographic properties of synthesized CuO, synchrotron X-ray diffraction (SXRD) was also utilized for characterization. The SXRD characterizations were performed at the BL19B2 beamline of the SPring-8 synchrotron facility in Hyogo, Japan, using a Si (111) monochromator to direct 30 keV X-rays with a

wavelength of 0.413269 Å. The intensity of the incident X-ray beam was measured in an ionization chamber filled with 99.99% pure nitrogen gas. Powder samples were placed in a 0.3mm inner diameter Lindermann capillary tube, and the diffracted X-rays were collected by a two-dimensional PILATUS-300K detector (DECTRIS AG, Baden-Daettwil, Switzerland) situated approximately 270.23 mm from the sample. In situ SXRD experiments on CuO-400 were conducted to examine its crystallographic parameters under rapid in situ temperatures of − 100, 0, 25, 100, 200, 300, 400, 500, 600 °C. In situ SXRD data of CuO-400 powdered sample were obtained using X-rays of wavelength approximately 0.495939 Å (X-ray energy ≈ 25 keV) in the scattering angle range from 2° to 85° using MYTHEN detectors installed in the high-throughput Polaris diffractometer at BL19B2. Additionally, laser Raman spectroscopy (LRS) was performed on powdered samples using a Renishaw Invia Raman spectrometer, scanning from 100 to 1000 cm^{-1} at room temperature. X-ray Photoelectron Spectroscopy (XPS) was performed on powdered samples with a Thermo Scientific™ ESCALAB Xi^+ (Thermo Fisher Scientific, Waltham, MS, USA) using Mg Kα radiation (hν = 1253.6 eV). Thermo gravimetric analysis (TGA) of as-synthesized CuO-25 was performed on a NETZSCH STA 2500 Regulus thermal analyzer. The optical properties of the powdered samples were analyzed using a UV–Vis–NIR spectrometer (Shimadzu UV–Vis. 2450, Shimadzu Corporation, Tokyo, Japan) in reflectance mode over a wavelength range of 300–900 nm, with spectral-grade $BaSO_4$ serving as the reference material.

Electrochemical characterization CuO electrodes

CuO electrodes were fabricated by tape casting a mixture that included the synthesized CuO powder (70 wt%), acetylene black (20 wt%), and polyvinylidene fluoride (PVDF) as a binder (10 wt%) in *N*-methyl pyrrolidinone (NMP) as the solvent [28]. This slurry was evenly applied onto the Cu foil current collector using the doctor blade method. It was then dried in a vacuum oven at 80 °C for 12 h. The current–voltage characteristics of the fabricated CuO anode were performed using an electrochemical workstation (Biologic Science Instruments SAS–VMP3) within a voltage range of − 0.5 to + 0.5 V, with a scan rate of 0.1 mV s^{-1}. Coin cells (type CR-2032) were assembled in an argon-filled glove box (< 1 ppm O_2 and H_2O) using the prepared anode electrodes, Li-foil (Sigma-Aldrich) as the reference and counter electrodes, Cellgard 2600 as the separator, and a non-aqueous electrolyte composed of 1 M $LiPF_6$ in ethylene carbonate and dimethyl carbonate (1:1 wt%). Galvanostatic charge–discharge tests were conducted using a battery testing system (Model-CT2001A, Landt Instruments, USA) at a rate of C/5 within a voltage range of 0.01–3.0 V (versus Li/Li^+) at room temperature (25 °C). Cyclic voltammetry (CV) was performed using a VMP3-based Biologic electrochemical workstation, between the potentials of 0.01 and 3.0 V at a scan rate of 0.1 mV s^{-1}.

Result and discussion

Material characterization

Crystallographic properties

The synthesized all these CuO powder samples were calcined at different temperatures in the range from 200 to 600 °C. The obtained XRD for CuO-25, CuO-200, CuO-400, and CuO-600 is shown in Fig. 1a. The well-defined diffraction peaks indicate the formation of a highly crystalline product. The diffraction peaks are observed at 2θ = 32.47°, 35.52°, 38.72°, 48.71°, 53.39°, 58.12°, 61.48°, 66.20°, 68.02°, 72.47°, and 75.20°, corresponding to (110), (002), (111), (210), (020), (202), (121), (301), (113), (311), and (203) planes, for CuO-25, CuO-200, CuO-400, and CuO-600 anode materials, respectively [12]. All these diffraction peaks in Fig. 1a are identical to the monoclinic symmetry of CuO (space group C2/c, JCPDS Card No. 48-1548) [32]. Furthermore, there is no evidence for the existence of residual or secondary phases such as Cu_2O, $Cu(OH)_2$, and Cu. It confirms the successful formation of high-purity CuO. However, with an increase in the calcination temperature, the intensity of the XRD peaks increases and the peaks become sharper, accompanied by a decrease in the FWHM (full width at half maximum), indicating an improvement in the crystallinity of the CuO anode material.

CuO is a conversion-type anode material. Therefore, it undergoes a reversible conversion reaction during its cycling process as follows, $CuO + 2Li^+ + 2e^- \leftrightarrow Cu + Li_2O$. According to the above reversible conversion reaction, CuO is

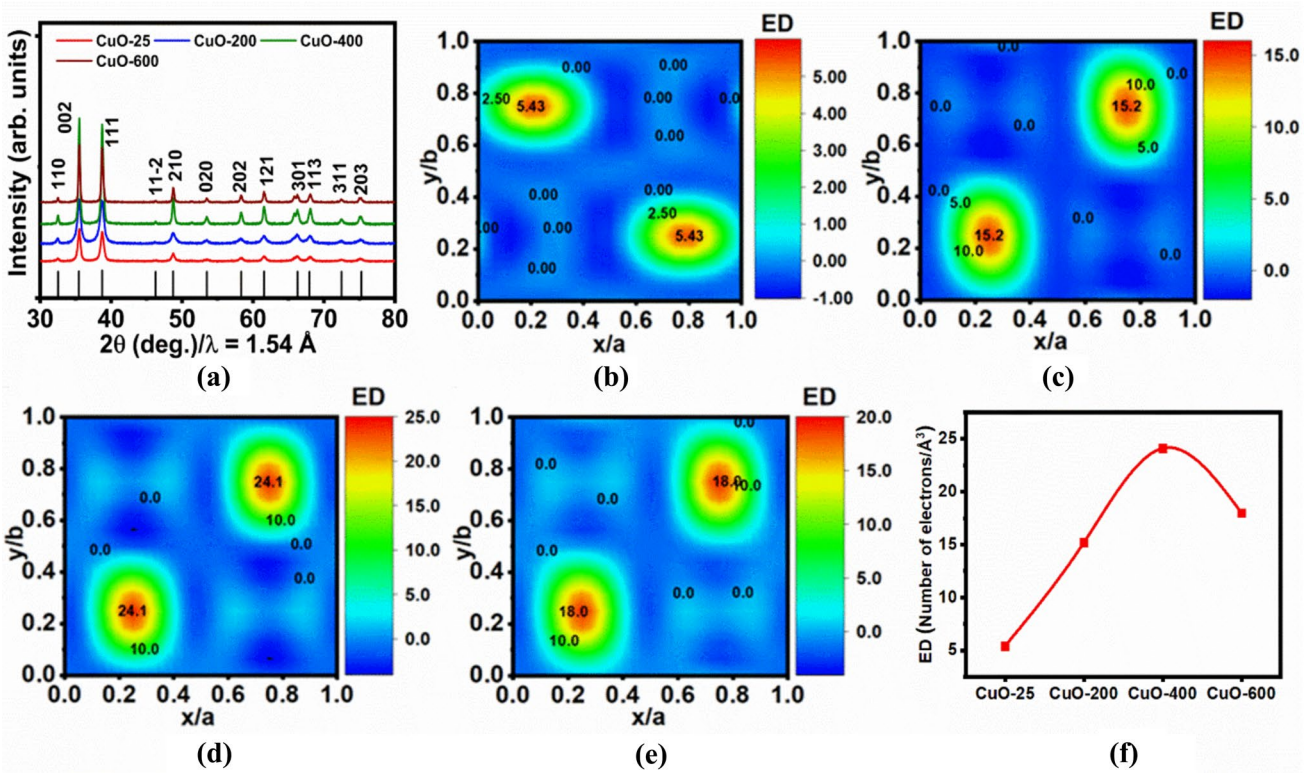

Figure 1 **a** Laboratory XRD pattern obtained for CuO-25, CuO-200, CuO-400, and CuO-600 anode materials. **b** 2D view of electron density distribution CuO-25 anode materials. **c** 2D view of electron density distribution CuO-200 anode materials. **d** 2D view of electron density distribution CuO-400 anode materials. **e** 2D view of electron density distribution CuO-600 anode materials. **f** Maximum electron density value variation for the CuO-25, CuO-200, CuO-400, and CuO-600 anode materials

reduced to metallic Cu during the discharging process, and Cu is reoxidized, reforming CuO during the charging process. Both conduction and valence band electron density in the CuO crystal structure are more important for the productive reversible conversion reaction of CuO anode due to the governing of electronic properties. Hence, both of the valence and conduction band electron density of CuO have a critical impact on its electrochemical performance when it is used as an anode electrode [34]. The distribution and availability of electrons in the valence band influence the conversion mechanism, affecting the cycling process and its overall electrochemical performance. A higher value of valence band electron density, particularly near the Fermi level, indicates a greater availability of electrons for the conversion mechanism at the anode electrode. Furthermore, the conduction band electron density is vital for enhancing electrochemical performance. A higher conduction band electron density in CuO facilitates electron transport faster within the material, resulting in improved electrochemical performance [35]. Therefore, investigating the electron density distribution in CuO is essential for its use as an anode in LIBs. Figure 1b–f shows 2D views of the electron density distribution of as-synthesized CuO-25 and calcined CuO-400 anode material crystal structures, derived from XRD Rietveld refinement (utilizing GFourier-FullProf). The Fourier program evaluates the scattering density within the unit cell of a crystal, regardless of its symmetry. GFourier-FullProf employs a Fast Fourier Transform (FFT) subroutine to advance the computation of the following expression [36]:

$$\rho(r) = \frac{1}{V}\sum_{H} F(H)\exp\{2\pi i(H\cdot r)\}$$

In this context, V denotes the volume of the unit cell, H denotes a reciprocal lattice vector, and r indicates a vector position within the unit cell. $F(H)$

denotes complex Fourier coefficients used to perform different types of Fourier syntheses. The unit of $\rho(r)$ is derived by dividing the units of $F(H)$ by those of V. For example, if $F(H)$ is expressed in electron units (the standard absolute units for X-ray diffraction) and V in $Å^3$, then $\rho(r)$ is computed as Number-of Electrons/$Å^3$. GFourier–FullProf calculates the total electron density, encompassing both valence and conduction band electron densities, based on the structural model refined through the Rietveld method [37]. Figure 1f shows the peak electron density distribution with different calcination temperatures. Altogether, from Fig. 1, it reveals that higher electron density distributions are concentrated around Cu atoms across all samples. Furthermore, the overall improved electron density distribution observed in CuO-400 confirms the improvement of both the conduction band and valence band electron density distribution. Therefore, the CuO-400 anode holds a high potential for improved electrochemical performance.

For the electrochemical performance of anode materials, ionic conductivity and structural stability are decisive and critical characteristics, particularly for conversion-type electrodes, for enhancing battery performance mainly capacity, cycle life, and rate capability [38]. Ionic conductivity and structural stability of anode materials significantly depend on stacking fault probability (SFP), lattice strain, crystallite size, and dislocation [39]. Too high or low values of SFP, lattice strain, crystallite size, and dislocation can be beneficial by enhancing ionic conductivity while showing the lower structural stability during cycling [30, 36, 37, 39]. The optimal value of SFP lattice strain, crystallite size, and dislocation depends on the type of material and desired battery performance characteristics. Therefore, it is important to investigate the influence of the above-mentioned structural properties of CuO with calcination on its electrochemical performance.

Stacking fault probability (SFP), denoted by α, is a measure of the disorder in the regular stacking of atomic layers in a crystal. It is determined from the shifts and broadening of peaks in X-ray diffraction (XRD) patterns that arise from these faults. The SF probability (α) is related to the peak shift, ($\Delta 2\theta$), following equation [40]:

$$\alpha = \left[2\pi^2/45\sqrt{3}\tan\theta\right] \cdot 2\theta$$

where θ is Bragg angle of the diffraction peak. A higher value of α indicates a greater density of faults in the material`s crystal structure. Figure 2a shows the stacking fault probability (SFP) variation of the crystallographic reflection planes of (002), (111), (210), (202), and (301) for CuO-25, CuO-200, CuO-400, and CuO-600 anodes with calcination temperature. According to this study, higher value of SFP has been shown along the <002> crystallographic direction for the CuO-400 anode material. SFP has been decreased along the <111> , <210> , <202> , and <301> crystallographic directions for the calcination temperature.

Lattice strain is an important material property. Electronic band structure and chemical reactivity of materials strongly depend on lattice strain, which is commonly analyzed using the Williamson–Hall uniform deformation model (WH-UDM), applied to X-ray diffraction patterns. The XRD peak broadening is attributed to two main factors: finite crystallite size and lattice strain. The peak broadening (β_D) due to crystallite size (D) is given by the Scherrer equation [41–43]:

$$\beta_D = \frac{K\lambda}{D\cos\theta}$$

Here, K is a constant equal to 0.90, λ is the wave length of the incident X-ray, D is the crystallite size, and θ is the Bragg angle. The broadening from lattice strain (ε) arises from crystal imperfection and distortions, such as the displacements of atoms from ideal positions [43]. It is expressed as a function of the lattice strain by the following relationship [44, 45]:

$$\beta_\varepsilon = 4\varepsilon\tan\theta$$

The total peak broadening is a sum of these two contributions [41, 46],

$$\beta_{hkl} = \beta_\varepsilon + \beta_D$$

By substituting the individual components, the equation becomes:

$$\beta_{hkl} = \frac{K\lambda}{D\cos\theta} + 4\varepsilon\tan\theta$$

This expression is rearranged into the linear form of the Williamson–Hall equation:

$$\beta_{hkl}\cos\theta = 4\varepsilon\sin\theta + \frac{K\lambda}{D}$$

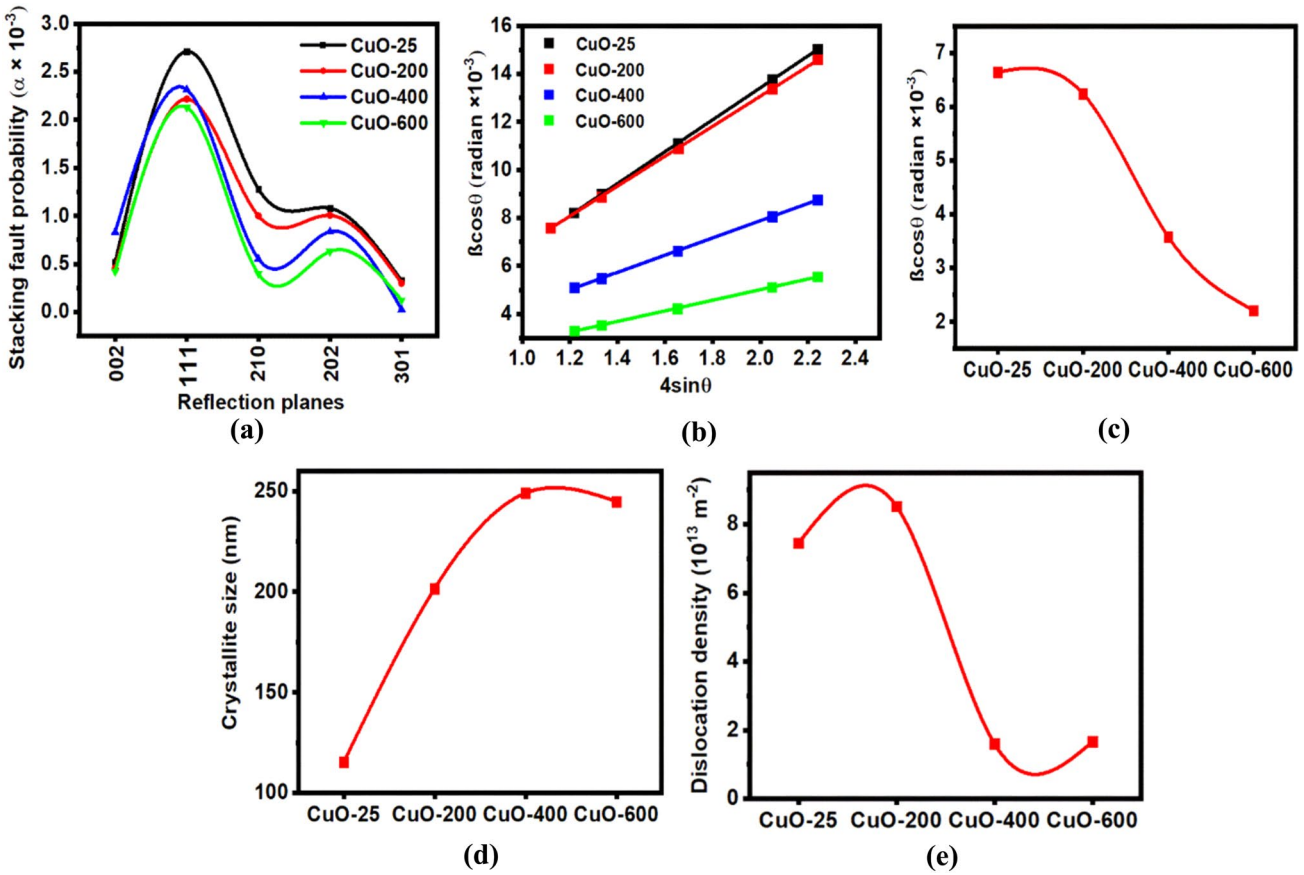

Figure 2 **a** Stacking fault probability (SFP) variation of the crystallographic reflection planes of (002), (111), (210), (202), and (301) for the CuO-25, CuO-200, CuO-400, CuO-600 anode materials. **b** William–Hall plot for the CuO-25, CuO-200, CuO-400, and CuO-600 anode materials. **c** Lattice strain variation for CuO-25, CuO-200, CuO-400, and CuO-600 anode materials. **d** Crystallite size variation for CuO-25, CuO-200, CuO-400, and CuO-600 anode materials. **e** Dislocation density variation for CuO-25, CuO-200, CuO-400, and CuO-600 anode materials variation with calcined temperatures

Both lattice strain and crystallite size are obtained using the slope and the *y*-intercept of the linear plot of the data. In this study, we have discussed the influence of lattice strain of CuO due to the calcination of chemical precipitated CuO on the electrochemical performance of the CuO anode. As know, no one has reported this kind of study for CuO anode in LIBs. Figure 2b shows the William–Hall plot for CuO due to the calcination temperature. It can be observed that the lattice strain of CuO has been reduced with the calcination temperature. Reducing the lattice strain in anode materials can better accommodate volume changes during the cycling process by minimizing the formation of cracks and other structural defects that lead to degradation. In contrast, over-reducing lattice strain in anode material during a conversion reaction can be disadvantageous to battery performance, including capacity loss, reduced cycle life, and increased internal resistance. Figure 2c shows the lattice strain variation for CuO-25, CuO-200, CuO-400, and CuO-600 anode materials according to this study. It can be observed that lattice strain decreases with the increasing of calcination temperature.

Crystallite size is the mean size of the well-arranged crystalline areas within a material and is often determined using XRD, which measures peak broadening to calculate crystallite size.

$$D = \frac{K\lambda}{\text{Intercept}}$$

Figure 2d shows the crystallite size variation of CuO with calcination temperature. It appears that the crystallite size has increased with calcination temperature, with CuO-400 anode material showing

the highest value. Crystallite size is an influential characteristic parameter for the electrochemical performance. A higher crystallite size generally improves faster cycling performance, though can negatively impact cycle life [30, 47]. Conversely, smaller crystallite sizes can enhance cycle life; nevertheless, they hinder faster cycling performance [48]. Dislocation density represents the concentration of line defects within a crystal structure. Dislocation density (δ) was determined by the following equation $\delta = 1/D^2$ [49] where D is the crystallite size. A higher value of dislocation density implies more dislocations are present in the material. It directly impacts the mechanical and electronic properties of the material. Figure 2e shows the dislocation density variation of CuO with calcination temperature. Linear defects in the crystal structure can act as additional active sites for lithium ions to store and create new pathways for ions and electrons to move during cycling performance. In anode for LIBs, a high or low dislocation density can be beneficial. An excessively high or low value of linear defect density can negatively impact for the electrochemical performance by increasing resistance or causing degradation. According to the present investigation of structural analysis, all calcined CuO materials have shown significant, promising electrochemical performance. However, the CuO-400 anode material reported the best electrochemical performance. It could be ascribed due to a lower value of stacking fault probability, leads to better mechanical stability.

SXRD technique can provide more accurate structural information in comparison with laboratory XRD. Figure 3a displays the SXRD profile, obtained for the CuO-25 and CuO-400 anode materials. It exhibited reflection peaks at 10.34°, 11.28°, 12.26°, 14.53°, 15.26°, 16.04°, 16.66°, 18.02°, 18.96°, 20.26°, 20.77°, 21.93°, and 22.62° due to (110), (002), (111), (112), (210), (020), (202), (121), (301), (220), (311), and (004), respectively. Further, the SXRD analysis excluded the presence of any residual or secondary phases in the prepared CuO, in agreement with the laboratory XRD analysis. According to the electron density distribution analysis via SXRD Rietveld refinement, the highest electron density distribution can be appeared for the CuO-400 anode material due to calcination of 400 °C as discussed in laboratory XRD refinement. In addition, SFP variation along the <111>, <210>, <202>, and <301> crystallographic directions is lower for CuO-400 compared to CuO-25 anode material, in agreement with the above discussion using laboratory XRD. Values of lattice strain, crystallite sizes, and dislocation density are calculated for CuO-25 and CuO-400 anode material with the use of SXRD. Calculated values are shown in Table 1.

The obtained Raman spectra for the as-synthesized CuO-25 and CuO-400 anode materials are presented in Fig. 4. The Raman spectra exhibit $A_g + 2B_g$ Raman active modes of CuO. A_g associated with the CuO bond involves oxygen atoms vibrating along the b-axis. This movement is a stretching or phase rotation of the bond [50]. The first B_g mode is related to the bending of CuO, and the second B_g mode corresponds to the symmetrical stretching of oxygen, perpendicular to the b-axis [50, 51]. The Raman spectra of as-synthesized CuO-25 and CuO-400 anode material show three firm peaks at 277.0, 324.0, and 610.0 cm^{-1}, which correspond to the A_g, B_{1g}, and B_{2g} characteristic modes of CuO with monoclinic crystal symmetry. The B_{1g} mode involves the vibration of oxygen atoms perpendicular to the b-axis in the crystal. The B_{2g} mode in CuO is a vibrational mode that provides information about the structural properties of CuO, such as phase transitions and strain effects. According to this study, there are no active modes related to the existence and formation of the secondary phase in as-synthesized CuO-25 and calcined CuO-400 anode materials. The peak intensity of a Raman spectrum is directly related to the concentration of the corresponding vibrational mode. CuO-400 anode material shows higher peak intensities for A_g, B_{1g}, and B_{2g} for Raman modes compared to as-synthesized CuO-25. The formation of additional CuO bonds vibrating along and perpendicular to the b-axis is attributed to the more crystalline structure resulting from calcination, as discussed in XRD and SXRD. Furthermore, the formation of a greater number of CuO bonds in a CuO crystal structure generally improves its stability, reactivity, and catalytic properties, potentially improving applications, including catalysis, energy storage, and sensing.

The thermal stability of crystallographic phases in anode materials is significant for the safe and reliable continuing operation of rechargeable batteries. In 2003, Wu et al. reported the correlation between electrochemical characteristics and thermal stability for LIBs [52]. Allcorn et al. have studied the thermal behavior of Cu_2Sb anode electrode materials in 2022 [53]. In this study, the calcined CuO-400 anode material at 400 °C exhibited the best electrochemical

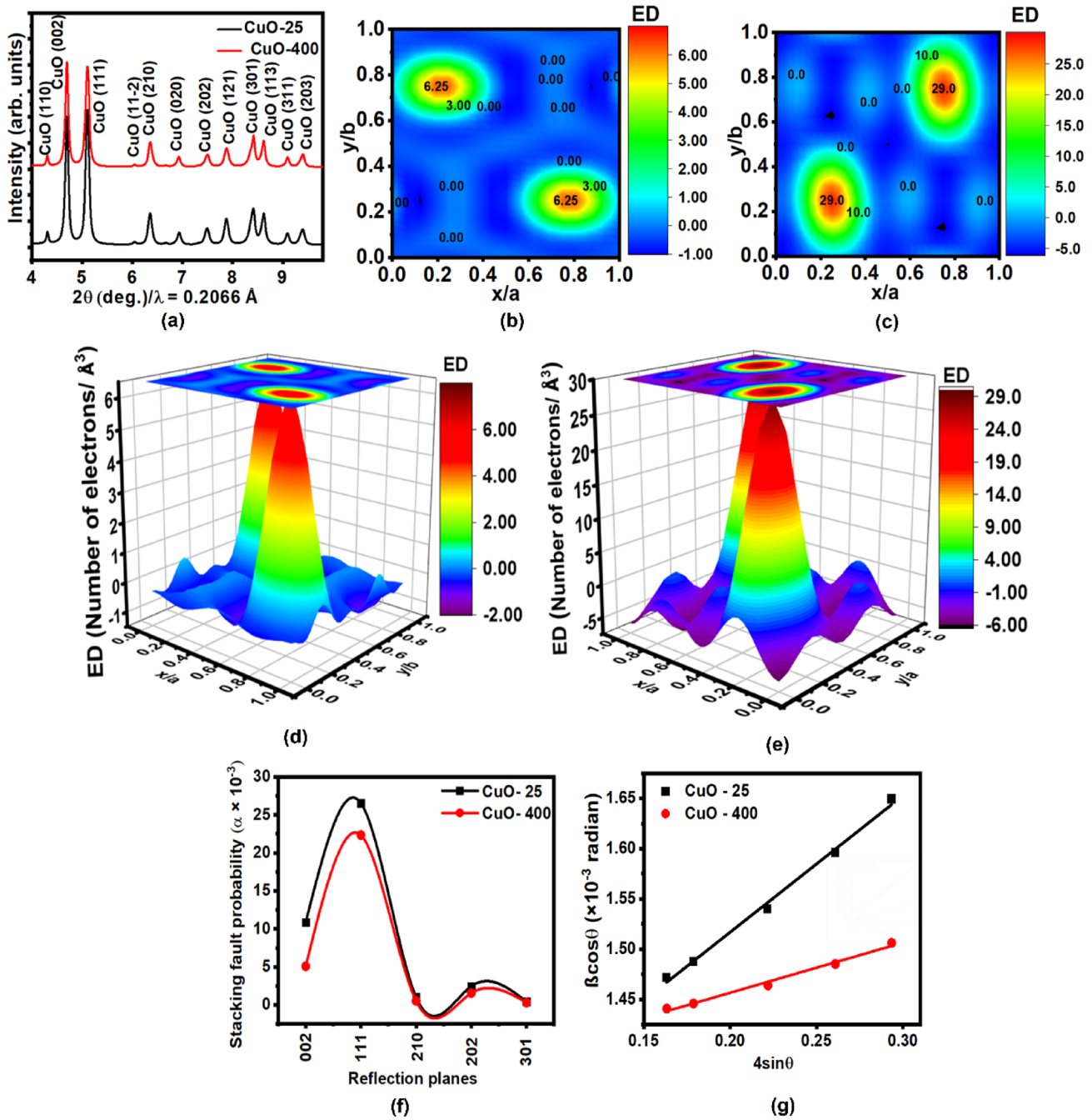

Figure 3 **a** SXRD pattern obtained for CuO-25 and CuO-400 anode materials. **b** 2D view of electron density distribution for as synthesized CuO-25 anode material. **c** 3D view (spatial variation) of electron density distribution for as synthesized CuO-25 anode material. **d** 2D view of electron density distribution for CuO-400 anode material calcined at 400 °C. **e** 3D view (spatial variation) of electron density distribution for CuO-400 calcined at 400 °C. **f** Stacking fault probability (SFP) variation of the crystallographic reflection planes of (002), (111), (210), (202), and (301) for the as synthesized CuO-25 and CuO-400 anode materials. **g** William–Hall plot for the CuO-25 and CuO-400 anode materials

performance. Consequently, the thermal stability of the crystallographic phase in CuO-400 anode material was investigated via taking the in situ SXRD characterization for the in situ temperatures of -100, 0, 25, 100, 200, 300, 400, 500, and 600 °C as shown in Fig. 5a. The atomic plane of (111) is directly related to

Table 1 Lattice strain, crystallite size, and dislocation density values of as-synthesized CuO and calcined CuO at 400 °C

Materials	Lattice strain (10^{-3}) radian	Crystallite size (nm)	Dislocation density (10^{13})
As-synthesized CuO	1.36	106.4	8.52
Calcined CuO at 400 °C	0.49	115.8	7.75

the *a*, *b*, and *c* axes. Hence, stretching or compression in the directions *a*, *b*, and *c* axes of the structure is determined due to the peak position shift of the atomic plane. In this study, the peak position of the atomic plane (111) in Fig. 5c has shifted to a lower degree, confirming the elongation of the crystal structure in *a*, *b*, and *c* directions as the in situ temperature increase from -100 to 600 °C. Figure 5d–g shows the variation of lattice parameters along the a, b, and c axes, and the volume of the crystal structure, indicating the expansion of the crystal structure. CuO crystal structure shows lattice parameter values and crystal structure volume of 4.6853, 3.4241, 5.1283, and 81.153 $Å^3$, respectively, for room temperature of 25 °C. According to Fig. 5d–g, lattice parameter values and crystal structure volume of the crystal structure of CuO are 4.6819 Å, 3.4224 Å, 5.1237 Å, and 80.9526 $Å^3$ for the in situ temperature of -100 °C. These values confirmed the contraction of the CuO crystal structure, with percentages of 0.07257%, 0.0511%, 0.0897%, and 0.24694% along the *a*, *b*, *c*, axes and volume. On the other hand, the crystallographic parameters of CuO have been increased due to an increase of in situ temperature, which is higher than room temperature. For the in situ temperature of 600 °C, lattice parameter values and crystal structure volume of crystal structure of CuO are 4.7107, 3.4398, 5.1543, and 82.4951 $Å^3$, indicating the expansion of CuO crystal structure with the percentages of 0.54212%, 0.45705%, 0.50699% and 1.65379% along *a*, *b*, *c*, axes and volume. Contraction or expansion of anode material with temperature affects the electrochemical performance and exhibits safety issues. Nonetheless, it is important to mention that the existence of CuO phases within the in situ temperature range of -100 to 600 °C is a considerable advantage of CuO anode for LIB applications. The existence of CuO phases at higher temperatures has the potential to offer some performance benefits, due to the improved kinetics of

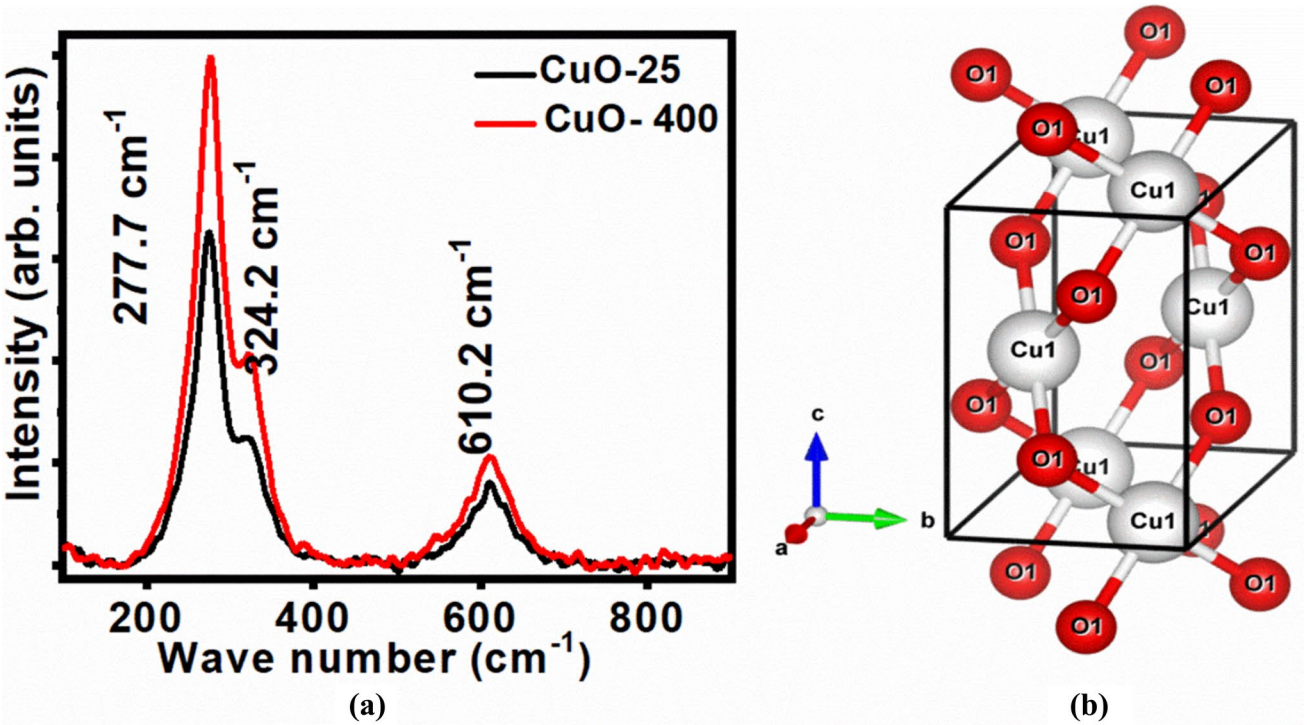

Figure 4 **a** The obtained Raman spectrum for as-synthesized CuO-25 anode material and CuO-400 anode material calcined at 400 °C. **b** Monoclinic crystal of CuO anode materials

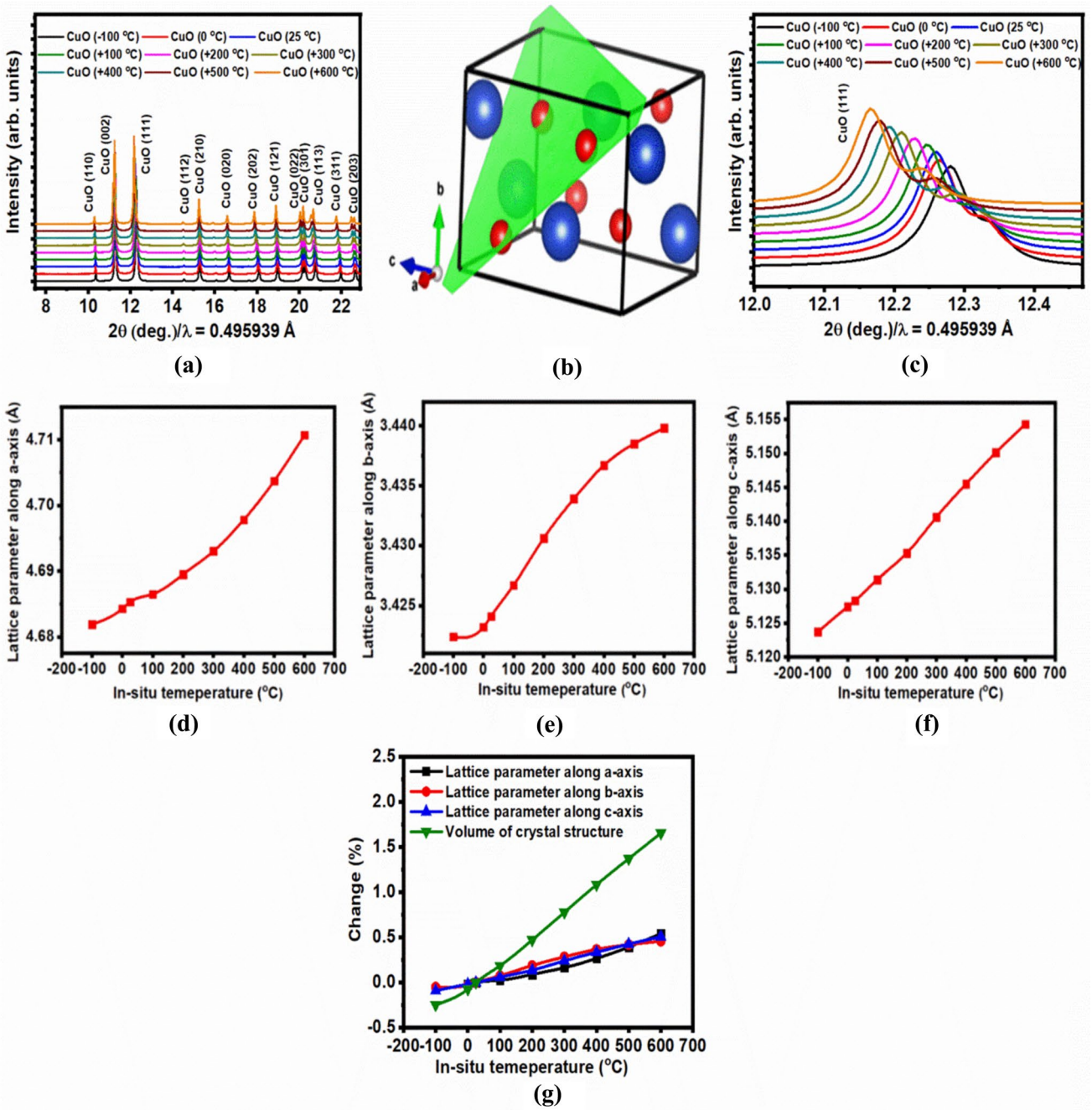

Figure 5 **a** In-situ SXRD characterizations for CuO-400 anode material calcined at 400 °C. **b** Atomic plane of (111) monoclinic crystal of CuO. **c** Magnified region of 111 plane. **d** Lattice parameter variation along a-axis with in-situ temperature. **e** Lattice parameter variation along the *b*-axis with in-situ temperature. **f** Lattice parameter variation along the *c*-axis with in-situ temperature. **g** Variation of volume of crystal structure variation with in-situ temperature. **h** Percentage-wise change of lattice parameters with in-situ temperature

lithium-ion diffusion and reduced resistance, leading to faster cycle performance. They also accelerate undesirable side reactions and degrade the electrode material stability, shortening the lifespan of the battery at high temperatures. In contrast, low temperatures lead to slow cycling performance because of slow transport of ion. Hence, further research studies are

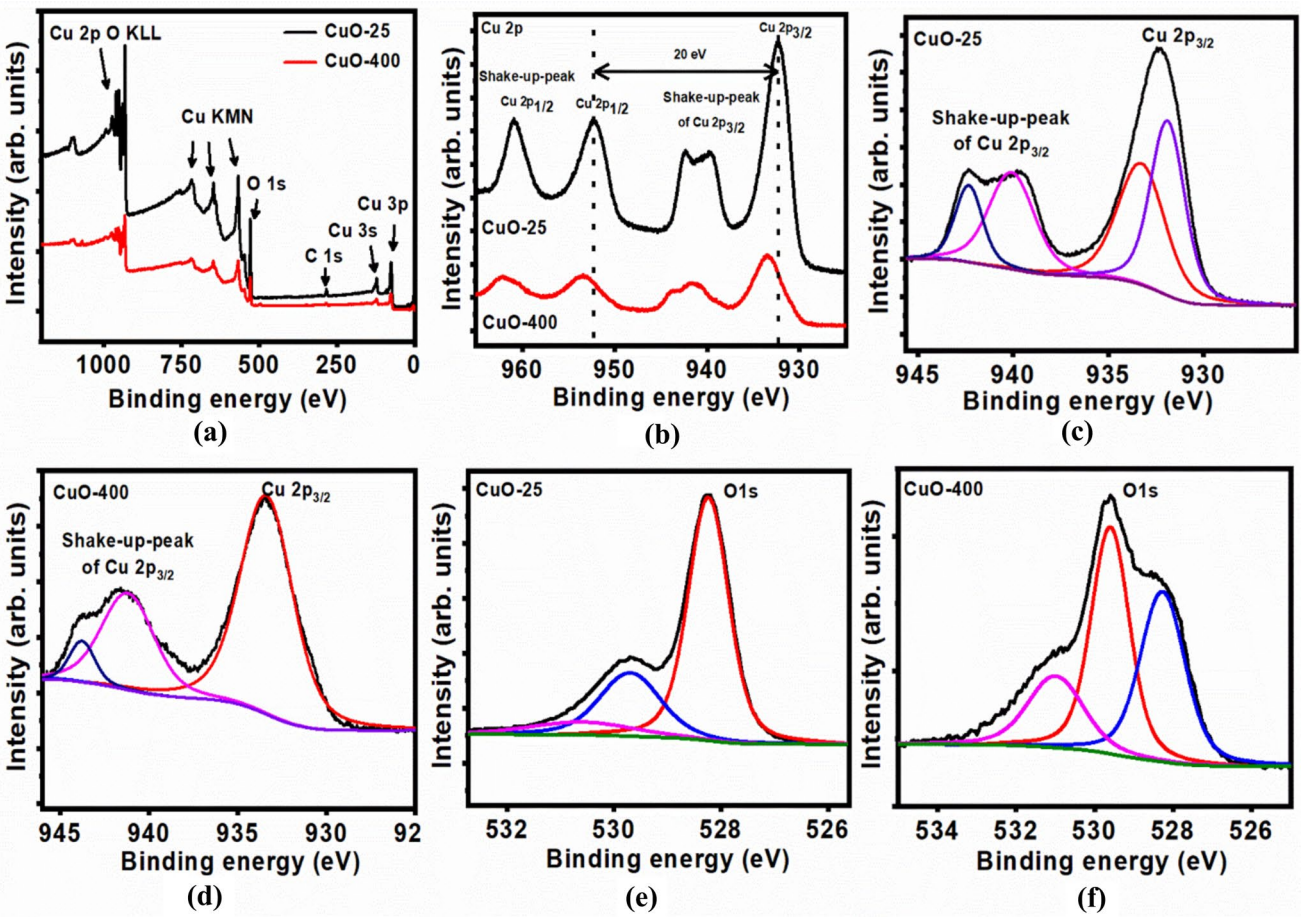

Figure 6 **a** Survey XPS spectra of as-synthesized CuO-25 and calcined CuO-400 at 400 °C. **b** The Cu 2*p* region of the XPS spectra of as-synthesized CuO-25 and calcined CuO-400 at 400 °C. **c** Curve-fitting spectrum of Cu $2p_{3/2}$ of as-synthesized CuO-25 anode materials. **d** Curve-fitting spectrum of Cu $2p_{3/2}$ of calcined CuO-400 anode materials at 400 °C. **e** Curve-fitting spectrum of O1s of as-synthesized CuO-25 anode materials. **f** Curve-fitting spectrum of O1s of calcined CuO-400 at 400 °C anode materials

important to investigate the optimal temperature range for long-term performance and safety.

Surface chemistry of CuO

The XPS survey spectra for the CuO-25 and CuO-400 anode materials were obtained to study a comparative analysis prior to and after calcination at 400 °C, as depicted in Fig. 6a. The survey spectra for both samples reveal the presence of Cu, O, and C elements, confirming the high purity of the CuO-25 and CuO-400 anode materials. As shown in Fig. 6b, the peak positions of Cu $2p_{3/2}$ and Cu $2p_{1/2}$ in CuO-400 have shifted, indicating an increase in binding energy. This shift can be attributed to changes in the surface chemical composition due to the calcination process. The difference in spin–orbit coupling energy between the two CuO samples is approximately 20 eV, which agrees with the characteristic + 2 copper oxidation state as reported in the previous literature [54]. The Cu 2*p* core-level spectra for CuO-25 and CuO-400 were analyzed using Gaussian curve fitting, as depicted in Fig. 6c, d. Prior to calcination, the Cu $2p_{3/2}$ peak is made up of two components: one at 937.7 eV, which is attributed to the Cu^{2+} phase and indicates the presence of OH^- groups on the surface of CuO, and another at 934.5 eV, characteristic of the CuO phase [55, 56]. Additionally, peaks at 944.4 and 946.9 eV correspond to Cu^{2+} satellite peaks, indicating the presence of $Cu(OH)_2$ primarily prior to calcination. In contrast, as shown in Fig. 6d, the Cu $2p_{3/2}$ peak after calcination at 400 °C displays a

single component at 934.3 eV, along with satellite peaks at 941.5 and 943.8 eV. This suggests that the calcination process is essential for achieving high-purity CuO. The O1s core-level spectra for the CuO-25 and CuO-400 anode materials were studied prior to and after calcination at 400 °C using a Gaussian curve-fitting method, as depicted in Fig. 6f, g. Prior to calcination, the primary O1s peak appears at 532.9 eV, attributed to $Cu(OH)_2$. Additionally, a weaker peak with a lower binding energy of

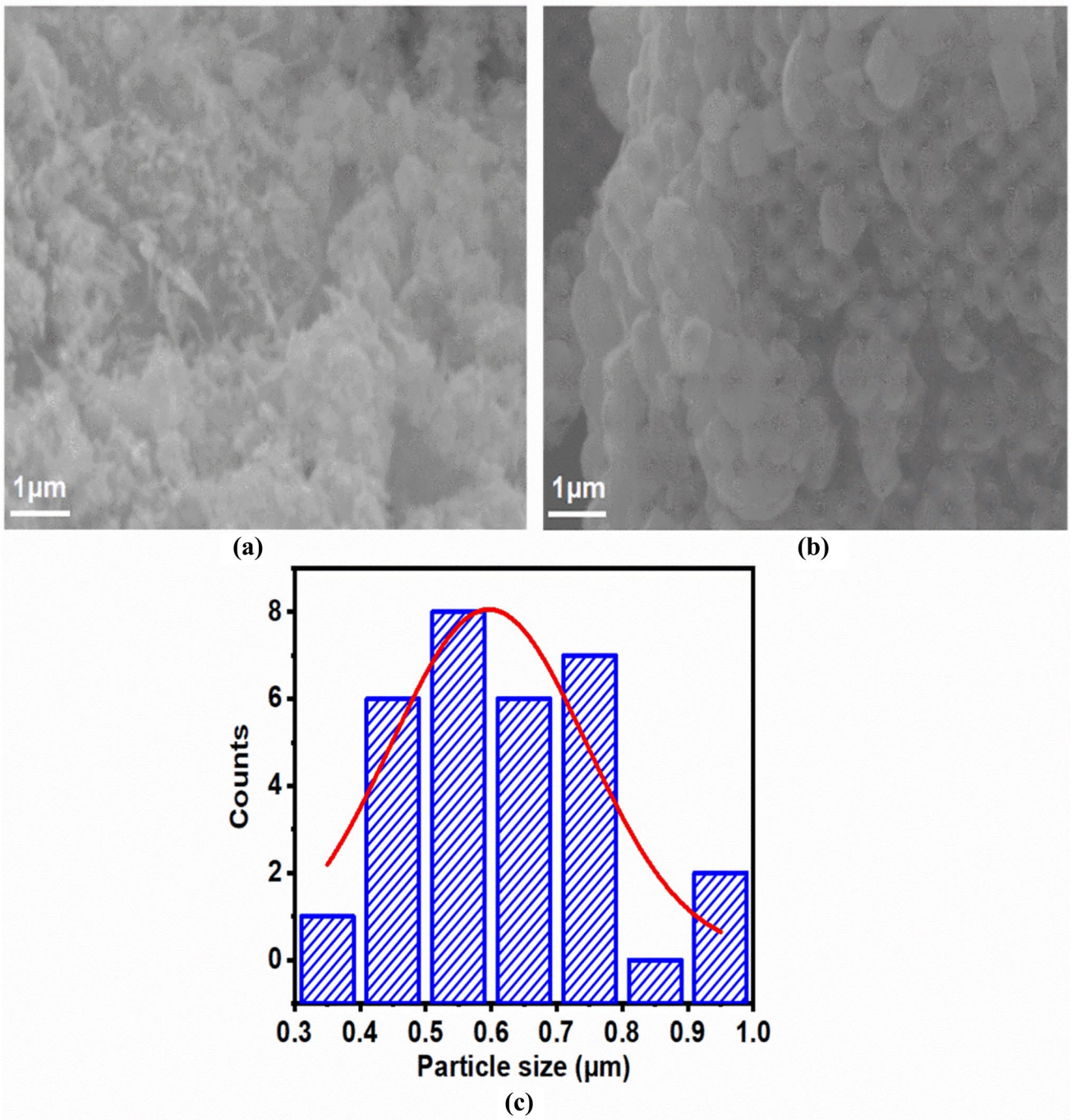

Figure 7 **a** SEM image of CuO-25 anode material. **b** SEM image of calcined CuO-400 anode material. **c** The particle size distribution of calcined CuO-400 anode material

529.1 eV is identified, which is associated with the presence on the surface of CuO, as noted in earlier studies [56]. After calcination, the main peak shifts to 529.6 eV, corresponding to the binding energy of CuO. Other peaks observed at 531.5 and 533.2 eV are due to oxygen and moisture from the air that has adsorbed onto the CuO surface [56].

Morphological analyses were performed for the as-synthesized CuO-25 and calcined CuO-400 anode materials using the SEM with a magnification of 30.0 K. As shown in Fig. 7a, CuO-25 anode material consists of tiny CuO clusters with more aggregation and conglomeration, and very short, tiny needles randomly distributed on the surface. According to Fig. 7b, the CuO-400 anode consists of round, granular particles of different sizes with distinct edges and aggregation. CuO-400 anode material shows the enhancement of the crystalline nature of CuO after calcination. Figure 7c presents the histogram of particle size distribution for the CuO-400 anode material. Calculated average particle size was 0.59 µm. The round and granular shape of the particles can enhance the contact surface area between the CuO/electrolyte interface, stimulating better reactions between the electrode and the electrolyte, and reducing the diffusion path for Li-ions. As a result, the calcined CuO-400 anode material at 400 °C enhances the overall electrochemical performance when utilized as an anode for LIBs.

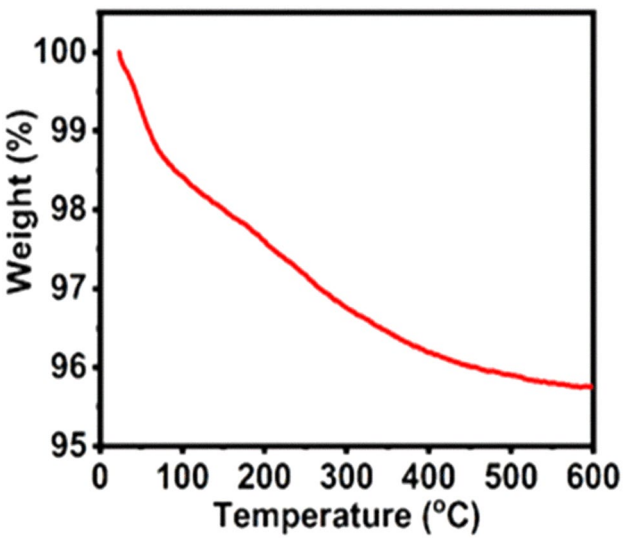

Figure 8 TGA curve for as-synthesized CuO-25 anode material

Thermogravimetric analysis (TGA)

The thermogravimetric analysis (TGA) curves for as-synthesized CuO-25 anode material is shown in Fig. 8. To study the thermal properties of the as-synthesized CuO-25 anode material, TGA was performed at a heating rate of 10 °C/min in an inert nitrogen atmosphere. TGA continuously measures the weight of samples as a function of temperature and time. It covers a temperature range from 25 to 600 °C. The TGA reveals important insights into the stability of the synthesized CuO at higher temperatures. The thermogravimetric analysis showed that the synthesized CuO exhibits remarkable thermal stability up to 600 °C. A slight weight loss of approximately 5% was observed up to 600 °C. It can be ascribed to the evaporation of water molecules that were adsorbed on the surface of the CuO particles. The significant thermal stability of synthesized CuO in this study is important for the cycle performance and safety of the CuO anode during cycling.

Optical and electrical properties

The diffuse reflectance UV–visible spectra of CuO-25 and CuO-400 anode materials were taken to investigate the band gap energy, which is crucial for LIBs due to the semiconducting properties of CuO. Tauc's plot method was used to determine the optical energy band gap of CuO-25 and CuO-400 by extrapolating the absorption spectrum measured by the spectrophotometer. Tauc's equation is shown as follows [57].

$$(\alpha h\nu)^{1/\gamma} = B\left(h\nu - E_g\right)$$

The diffuse reflectance UV–visible spectrum of CuO was taken for the CuO-25 and CuO-400 anode materials. According to the Kubelka–Munk (K–M) theory, reflectance data were transformed into absorption data mode.

$$F(R_\infty) = \frac{K}{S} = \frac{(1 - R_\infty)}{2R_\infty}$$

$R_\infty = \frac{R_{\text{sample}}}{R_{\text{standard}}}$ is the reflectance of an infinitely thick specimen, while K and S are the absorption and scattering coefficients, respectively. Putting $F(R_\infty)$ instead of α into the Tauc's equation

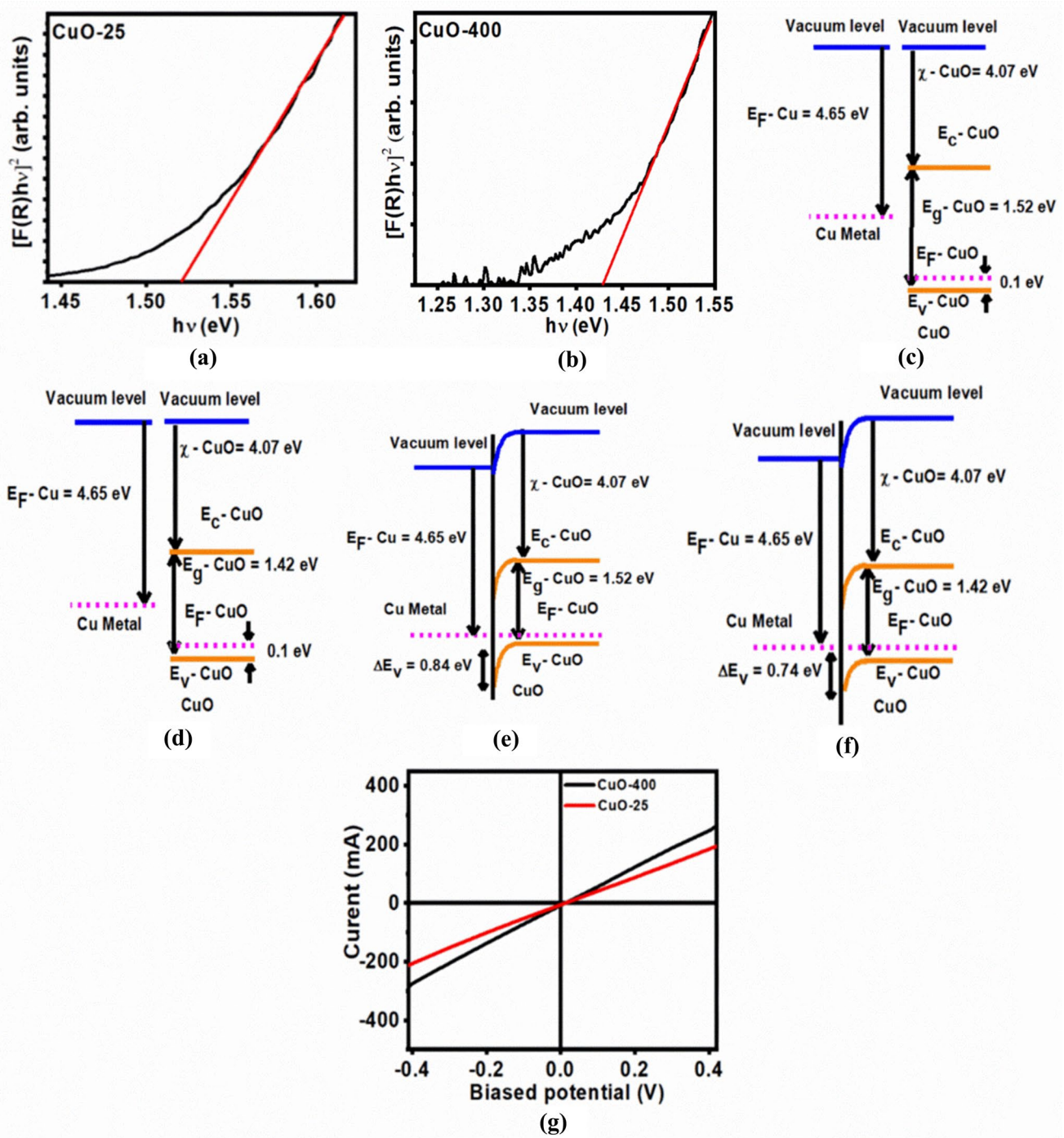

Figure 9 **a** Plot $(F(R)h\nu)^2$ as a function of photon energy of as synthesized CuO-25 anode material. **b** Plot $(F(R)h\nu)^2$ as a function of photon energy of calcined CuO-400 anode material at 400 °C. **c** Band diagram before formation the junction Cu/CuO-25 interface for as synthesized CuO-25 anode. **d** Band diagram before formation the junction Cu/CuO-400 interface of calcined CuO-400 anode at 400 °C. **e** Band diagram after formation the Schottky barriers Cu/CuO-25 interface for as synthesized CuO-25 anode. **f** Band diagram after formation the Schottky barriers Cu/CuO-400 interface of calcined CuO-400 anode at 400 °C. **g** Current–voltage characterization Cu/CuO-25 for as synthesized CuO-25 anode and Cu/CuO-400 anode

$$\left(F\left(R_\infty\right)\cdot h\nu\right)^{1/\gamma} = B\left(h\nu - E_g\right)$$

For direct band gap, $\gamma = \frac{1}{2}$

$$\left(F\left(R_\infty\right)\cdot h\nu\right)^{2} = B\left(h\nu - E_g\right)$$

Finally, the band gap energy of CuO-25 and CuO-400 is determined using Tac's equation through extrapolating the straight line of the plot of $[F(R) \times h\nu]^2$ versus incident photon energy $h\nu$. Figure 9a, b shows the plot of $[F(R) \times h\nu]^2$ versus incident photon energy $h\nu$ for CuO-25 and CuO-400, respectively. Computed band gaps were 1.52 and 1.42 eV for as-synthesized CuO-25 and calcined CuO-400 at 400 °C, respectively. A lower band gap value of CuO-400 can improve electrical conductivity and charge transfer kinetics, beneficial for its electrochemical performance as an anode in LIBs. Furthermore, electronic interfacial properties at Cu/CuO-25 and Cu/CuO-400 are important for the electrochemical performance of half-cells. The energy diagrams for the Cu/CuO-25 and Cu/CuO-400 interfaces are shown in Fig. 9c, d. The Schottky contacts are constructed at Cu/CuO-25 and Cu/CuO-400 interfaces as shown in Fig. 9e, f due to the misalignment of the Fermi level position of Cu, CuO-25, and CuO-400. Formation of this type of Schottky barrier impedes the transfer of electron between the copper current collector and the CuO anode material. Consequently, it reduces the electrochemical performance of CuO anode during cycling. Nonetheless, it can be appeared that the valence band offsets (ΔE_V, CuO-25/ΔE_V, CuO-400) are 0.84 and 0.74 eV for CuO-25 and CuO-400, respectively. Polymer binders and acetylene black as conductive additives were added to the CuO anode material for the CuO anode preparation. The electronic interfacial properties at the Cu/CuO-25 and Cu/CuO-400 interfaces depend on the mass ratio of active material, acetylene black, and polyvinylidene fluoride (PVDF) binder. The amount of conductive additive is sufficient to provide electrical conductivity in the CuO active material, facilitating, and electron movement via Cu/CuO-25 and Cu/CuO-400 interfaces during the cycling process by decreasing internal resistance and polarization within the anode [35]. The addition of a lower amount of acetylene carbon black improves the amount of active material content in the anode electrode. It leads to a reduction in the number of conductive pathways through the Cu/CuO interface, decreasing the overall electrochemical performance of the anode electrode [57]. In contrast, a high amount of acetylene carbon black enhances its electrical conductivity; however, it negatively impacts the electrochemical performance of the anode electrode due to the lower availability of CuO active material [57]. As a result, it leads to blocking the Li^+ diffusion pathways, reducing the electrochemical performance of the anode electrode. The initial investigation of this study revealed that the CuO anode exhibited the best electrochemical performance, composed of polyvinylidene fluoride (PVDF) binder and acetylene black in a mass ratio of 70:10:20 [28]. Thus, the CuO anode was fabricated for the subsequent studies of the current investigation employing the above-mentioned optimal mass ratio of 70:10:20. Figure 9g shows the obtained current–voltage characterization curves for Cu/CuO-25 and Cu/CuO-400 anodes. It shows the linear relationship between current and voltage without showing diode characteristics at the Cu/CuO-25 and Cu/CuO-400 interfaces. Hence, it confirms the formation of Ohmic contacts at Cu/CuO-25 and Cu/CuO-400 interfaces. According to Ohm's law, the lower electrode resistance value of 1.44 Ω shows the CuO-400 anode compared to the value of 1.88 Ω for the CuO-25 anode. It could be due to the reduced valence band offset at Cu/CuO-400 interface.

Table 2 Specific discharge and charge capacities of the CuO-25, CuO-200, CuO-400, and CuO-600 anodes

Electrode	Specific discharge capacity for the first cycle (mA h g^{-1})	Specific charge capacity for the first cycle (mA h g^{-1})	Specific discharge capacity for the 50th cycle (mA h g^{-1})	Specific charge capacity for the 50th cycle (mA h g^{-1})
CuO-25	1366.0	451.7	232.3	222.9
CuO-200	2100.7	522.9	342.7	340.3
CuO-400	2751.7	602.1	555.6	552.2
CuO-600	1004.3	244.8	300.8	300.4

Electrochemical performance

Galvanostatic cycle performance

The synthesized CuO powder samples were calcined at different temperatures, including 200, 400, and 600 °C, each maintained for 2 h, to identify the optimal conditions prior to further investigating the electrochemical performance of the developed CuO anode materials. The electrochemical performances reported for the CuO prepared at different calcination temperatures are presented in Table 2. The electrochemical performance results for the CuO prepared at the different calcination temperatures are summarized in Table 2. According to preliminary investigations, the CuO anode was found to exhibit significant electrochemical performance at a 400 °C calcination temperature. In contrast, the 200 and 600 °C calcination temperature showed inferior performance, particularly in terms of charge capacities during the first cycle and overall cycle life. Further investigations were performed on the as-synthesized (CuO-25) and calcined CuO (CuO-400) samples at 25 and 600 °C.

Figure 10a, b shows the charge–discharge capacities of the as-synthesized CuO-25 anode and calcined CuO-400 anode at 400 °C as a function of the number of cycles up to 50 cycles, respectively. The charge–discharge capacities of the CuO-25 and CuO-400 anodes gradually decrease with increased cycle number. CuO-25 and CuO-400 anodes exhibited the initial specific discharge capacities of 1366.0 and 2751.7 mA h g^{-1}, respectively. Initial cycles of CuO-25 and CuO-400 anodes have shown a significant capacity loss of 914.3 and 2149.6 mA h g^{-1}. These irreversible capacity losses of both anodes are due to the formation of SEI between the anode and the electrolyte interfaces as reported in previous literature [58]. Remarkably, the initial specific discharge and charge capacities that resulted in the present study are higher than

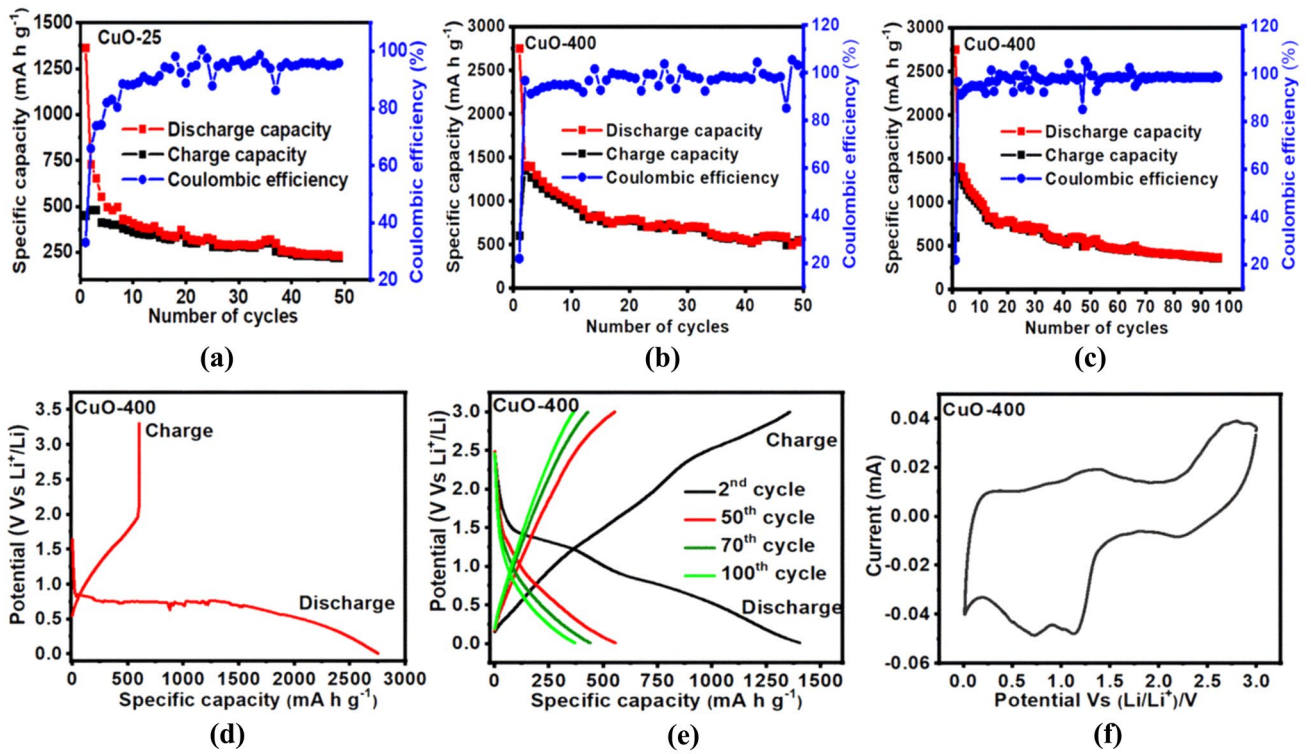

Figure 10 **a** Cycle performance versus cycle number of CuO-25 anode at a rate of 1.0 C up to the 50th cycle. **b** Cycle performance versus cycle number of CuO-400 anode at a rate of 1.0 C up to the 50th cycle. **c** Cycle performance versus cycle number of CuO-400 anode at a rate of 1.0 C up to the 100th. **d** Charge–discharge potential profiles of CuO-400 anode between the voltage range of 0.01 and 3 V at a rate of 1.0 C for the 1st cycle. **e** Charge–discharge potential profiles of CuO-400 anode between the voltage range of 0.01 and 3 V at a rate of 1.0 C for the 100th cycle. **f** Cyclic voltammograms of CuO-400 anode from 0.01 to 3.0 V (versus Li^+/Li) at a scan rate of 0.1 mV s^{-1} after 100th cycle

those of previously reported studies: nanochain CuO (1002.9 mA h g^{-1} at 0.1 C) [13], microsphere (1063.9 mA h g^{-1} at 0.1 C) [23], CuO nanotube (808.0 mA h g^{-1} at a rate of 0.1 C) [59], CuO nanodisc (971.0 mA h g^{-1} at a rate of 0.2 C) [60], CuO nanoplate (966.2 mA h g^{-1} at a rate of 1.0 C) [61], mulberry-like shape CuO (929.4 mA h g^{-1} at a rate of 1.0 C) [61] and pillow-shaped porous CuO (776.3 mA h g^{-1} at a rate of 0.1 C) [62]. Although the electrode exhibited lower Coulombic efficiencies of 48.0% and 24% for the CuO-25 and CuO-400 anodes in the first cycle, respectively, higher Coulombic efficiencies were observed in subsequent cycles, indicating the proper transfer of Li^+ and electrons between the anode and cathode.

The theoretical specific capacity of the CuO electrode is regarded as 674 mA h g^{-1}. The resulting specific capacity of the CuO-400 anode in the present study is considerably higher than that of its theoretically specific capacity mainly due to the factors such as formation of SEI, the reduction of adsorbed constituents on active material surfaces, and the initial formation of Li_2O during the first cycle as previously reported by Fernando et al. and Debbichi et al. [28, 50]. Furthermore, as shown in SEM analysis, the microstructural morphology of CuO-400 consists of granular particles of spherical nature having distinct edges in variable sizes. The resultant higher surface area could enhance the contact area at the CuO/electrolyte interface. The resultant higher surface area could enhance the contact area at the CuO/electrolyte interface. Hence, a considerably larger amount of may be stored at the interface during the first cycle. Consequently, it may have caused the resultant higher discharge capacity for the initial cycle than its theoretical value of 674 mA h g^{-1}. A similar behavior of higher initial specific discharge capacity than that of 674 mA h g^{-1} for CuO anode in LIB also reported in the following literature [13, 23, 28, 59–62].

After 50 cycles, CuO-25 and CuO-400 anodes delivered specific discharge capacities of 232.3 and 552.2 mA h g^{-1} with a Coulombic efficiencies of 98.0 and 99.4%, respectively. Specific discharge capacity of 552.2 mA h g^{-1} with a Coulombic efficiency of 99.4% indicates promising cyclic behavior due to calcination. Interestingly, it achieved more than 80% of the theoretical specific capacity of CuO anode. Furthermore, CuO-400 anode delivered better performance in the present study in comparison with those of previously reported CuO structures: nanochain CuO (611.9 mA h g^{-1} at a rate of 0.1 C after 30 cycles) [13], microsphere (429.0 mA h g^{-1} at 0.1 C after 50 cycles) [23], CuO nanodisk (290 mA h g^{-1} at a rate of 0.2 C after 20 cycles) [60], pillow-shaped Porous CuO (350.0 mA h g^{-1} at a rate of 0.1 C after 50 cycles) [62]. According to this present study, better cycle performance is shown for the CuO-400 anode. It could be due to the existence of a higher electron density distribution in the crystal structure. Moreover, as mentioned in the crystallographic study in Sect. "Crystallographic properties", structural properties such as SFP variation, lattice strain, crystallite size, and dislocation density values are crucial characteristics for the electrode material for their electrochemical performance. There is no specific linear relationship between those mentioned properties and electrochemical performance. It significantly depends on the material. Even though the engineered structural properties of electrode material are beneficial for their electrochemical performance, lower or higher values of structural properties are an advantage or disadvantage, depending on the material. This study reveals the values of structural properties that are formed due to the calcination at 400 °C is promising for CuO as an anode electrode in LIBs. To the best of the knowledge, no one have been investigated the effect of structural properties of CuO anode material due to the calcination process. Furthermore, according to the XPS analysis in Sect." Surface chemistry of CuO", the existence of $Cu(OH)_2$ was shown for the CuO-25 anode material. The CuO anode material can be negatively impacted by its instability during phase transformation during the cycling process. Consequently, the presence of $Cu(OH)_2$ can impede the anticipated rate of the conversion mechanism reaction at the CuO anode. Be that as it may, after calcination, XPS analysis confirmed the formation of high-purity CuO for CuO-400 without the existence of $Cu(OH)_2$, which is an advantage for CuO anode applications in LIBs.

According to Fig. 10c, a slight fluctuation in specific charge–discharge capacities can be observed for the CuO-400 anode. Hence, it is essential to conduct further research studies to develop as anode electrode for LIBs. Nevertheless, it exhibited better electrochemical performance as a novel anode material for LIBs. The cycling performance of the CuO-400 anode was extended to 100 cycles as shown in Fig. 10c. After 100 cycles, CuO-400 anode delivered specific discharge capacity of 364.2 mA h g^{-1} with a Coulombic

efficiency of 98%. Furthermore, Wang et al. have reported a hierarchical structure of CuO with specific discharge capacities of 575.0 mA h g^{-1} at a rate of 1.0 C over 100 cycles and 504.0 mA h g^{-1} at a rate of 2.0 C over 100 cycles. Their electrochemical performance is better than that of the present study. However, CuO was synthesized using a simple, inexpensive, high-safety, non-toxic, and environmentally friendly chemical precipitation technique for this study. This was attained without the use of high-toxicity or costly chemicals, costly instruments and multistep processes.

Figure 10d displays the discharge–charge potential profile of the first cycle for the CuO-400 anode. Accordingly, it showed three sloping potential ranges of 0.84–0.75 V, 0.75–0.47 V, and 0.39 –0.01 V. These three sloping potential ranges presumptive to the reduction of CuO to the intermediate composite copper oxide phase, further reduction to Cu_2O and finally decomposition into Cu fine particles and Li_2O, respectively, as discussed in previous literature [4, 6]. Figure 10e shows charge–discharge potential profiles for the CuO-400 anode up to the 100th cycle. It is observed that the shapes and continuity of the curves do not change significantly in the following cycles, implying good reversibility of the electrochemical reaction up to the 100th cycle for CuO-400 anode.

Figure 10f shows the cyclic voltammograms of the calcined CuO-400 anode recorded at a scan rate of 0.1 mV s^{-1} after the 100th cycle. During the cathodic sweep, three cathodic peaks can be seen at 2.2, 1.1, and 0.7 V. These peaks are associated with a multistep of electrochemical reactions, which include the formation of an intermediate solid solution phase ($Cu^{II}_{1-x}Cu^{I}_{x}O_{1-x/2}$) (where $0 < x < 0.4$), the reduction of CuO to Cu_2O, and ultimately the further reduction to Cu and Li_2O [4, 23]. Additionally, oxygen is released from the host structure, leading to the formation of oxygen ion vacancies. These oxygen ion vacancies are then stabilized by lithium ions to create the Li_2O phase. The anodic peaks reveal two significant oxidation peaks at approximately 1.3 and 2.7 V, indicating that a multistep electrochemical reaction occurs, involving the oxidation of Cu to Cu_2O and eventually to CuO. In addition, continuity of anodic and cathodic sweep of cyclic voltammograms confirms the proper working of the kinetic reaction after the 100th cycles. This study reveals the improvements in the electrochemical performance of the calcined anode. It is due to the enhancement of the electron density distribution in the crystal structure via calcination. Furthermore, this study has shown the importance of electron density distribution in the crystal structure for the CuO-based anode material. To the best of our knowledge, no one have been done this kind of investigation for CuO anode for LIBs.

Conclusion

This research focused on synthesizing CuO through a simple chemical precipitation method and optimizing its structural characteristics and electron density by calcination process to improve its electrochemical performance as an anode in LIBs. Accordingly, the overall enhanced electron density distribution observed in CuO-400. Higher value of SFP has been shown along the <002> crystallographic direction for the CuO-400. Lattice strain decreases with the increasing calcination temperature. CuO-400 anode material has the highest value of crystallite size, 115.8 nm, improving conversion mechanism reaction. Lower value of dislocation density showed for the CuO-400 anode, leading to better mechanical stability. Volume of the crystal structure contracted and expanded by 0.24694% and 1.65379% for the in situ temperature range from − 100 to 600 °C. Additionally, in situ synchrotron XRD confirmed the presence of a monoclinic crystal structure of CuO across a temperature range from − 100 to 600 °C, indicating the thermal stability of CuO phases. According to the electrochemical characterization, the CuO-400 anode material, calcined at 400 °C, achieved the highest initial specific discharge capacity of 2751.7 mA h g^{-1} at a rate of 1.0 C, better electrochemical performing the as-synthesized CuO as anode. CuO-400 anode exhibited a specific discharge capacity of 364.2 mA h g^{-1} and a Coulombic efficiency of 98% after 100 cycles. Thus, synthesizing CuO while adjusting the electron density structural properties is an effective strategy to enhance the electrochemical performance of CuO anode for LIBs.

Acknowledgements

Members of the National Centre for Advanced Battery Research of the National Institute of Fundamental Studies, Sri Lanka, are acknowledged. The authors are grateful for the facilities and other support given by the synchrotron XRD measurements were carried out

at SPring-8 with the approval of the Japan Synchrotron Radiation Research Institute (JASRI) under proposal nos. 2024A1761, 2025A1568 and 2025A1947.

Author contributions

W. T. R. S. Fernando, T. H. N. G. Amaraweera, and H.W.M.A.C. Wijayasinghe contributed to conceptualization, methodology, investigation, and writing-original draft; W. T. R. S. Fernando contributed to software; W. T. R. S. Fernando, T. H. N. G. Amaraweera, K.M.D.C. Jayathilaka, L. S. R. Kumara, and R.P. Wijesundera contributed to formal analysis; O. Seo, K. Osaka, O. Sakata, and H.W.M.A.C. Wijayasinghe contributed to resources; W. T. R. S. Fernando, K.M.D.C. Jayathilaka, L. S. R. Kumara, O. Seo, K. Osaka, O. Sakata, and R.P. Wijesundera contributed to data curation; T. H. N. G. Amaraweera, K.M.D.C. Jayathilaka, L. S. R. Kumara, O. Seo, K. Osaka, O. Sakata, R.P. Wijesundera, and H.W.M.A.C. Wijayasinghe contributed to writing—review and editing; T. H. N. G. Amaraweera and H.W.M.A.C. Wijayasinghe supervised the study; and H.W.M.A.C. Wijayasinghe contributed to project administration and funding acquisition. All authors have read and agreed to the published version of the manuscript.

Funding

This research was funded by National Center for Advanced Battery Research, National Institute of Fundamental Studies, Kandy 20000, Sri Lanka.

Data availability

Data are contained within the article.

Declarations

Ethical approval Not applicable.

Conflict of interest The authors declare no conflict of interest.

References

[1] Kim MC, Kim SJ, Han SB, Kwak DH, Hwang ET, Kim DM (2015) Cubic and octahedral Cu_2O nanostructures as anodes for lithium-ion batteries. J Mater Chem 3:23003–23010

[2] Zhang H, Yang Y, Ren D, Wang L, He X (2021) Graphite as anode materials: fundamental mechanism, recent progress and advances. Energy Storage Mater 36:147–170

[3] Winowatan PW, Selwyn S, Priyono B, Syahrial AZ (2021) Enhancing battery performance of $Li_4Ti_5O_{12}$ nanorod synthesized by hydrothermal method with Sn addition as anode material for lithium-ion battery. J King Saud Univ Eng Sci 33:396–403

[4] Deng Z, Ma Z, Li Y, Li Y, Chen L, Yang X, Wang H (2018) Boosting lithium-ion storage capability in CuO nanosheets via synergistic engineering of defects and pores. Front Chem 6:1–9

[5] Yi X, Qi G, Liu X, Depcik C, Liu L (2024) Challenges and strategies toward anode materials with different lithium storage mechanisms for rechargeable lithium batteries. J Energy Storage 95:112480

[6] Zhang W, Wang H, Zhang Y, Yang Z, Wang Q, Xia J, Yang X (2013) Facile microemulsion synthesis of porous CuO nanosphere film and its application in lithium ion batteries. Electrochim Acta 113:63–68

[7] Fang S, Bresser D, Passerini S (2020) Transition metal oxide anodes for electrochemical energy storage in lithium- and sodium-ion batteries. Adv Energy Mater 10:1–21

[8] Rahal A, Bouchama I, Ghebouli MA, Ghebouli B, Fatmi M, Alomairy S, Boudour S, Benlakhdar F, Chellouche M (2025) Optimization of structural and electronic properties in CuO/CIGS hybrid solar cells for high-efficiency, sustainable energy conversion. RSC Adv 15:23311–23318

[9] Bu IYY, Huang R (2017) Fabrication of CuO-decorated reduced graphene oxide nanosheets for supercapacitor applications. Ceram Int 43:45–50

[10] Zedan AF, Mohamed AT, El-Shall MS, Alqaradawi SY, Aljaber AS (2018) Tailoring the reducibility and catalytic activity of CuO nanoparticles for low temperature CO oxidation. RSC Adv 8:19499–19511

[11] Steinhauer S (2021) Gas sensors based on copper oxide nanomaterials: a review. Chemosensors 9:1–20

[12] Wang H, Liang T, Yu X, Zhao W, Xu R, Wang D, Liu Y (2016) Hydrothermal synthesis of well-crystallized CuO hierarchical structures and their direct application in high performance lithium-ion battery electrodes without further calcination. RSC Adv 6:96882–96888

[13] Wang P, Gou XX, XinS CFF (2019) Facile synthesis of CuO nanochains as high-rate anode materials for lithium-ion batteries. New J Chem 43:6535–6539
[14] Li C, Wei W, Fang S, Wang H, Zhang Y, Gui Y, Chen R (2010) J Power Sources 195:2939–2944
[15] Yuan W, Ye YT, Yang Y, Zhang XQ, Pan BY, Peng ZM, Wu ML, Qiu ZQ (2020) CuO nanoflowers/copper fiber felt integrated porous electrode for lithium-ion batteries. Sci China Technol Sci 63:2423–2434
[16] Zhang W, Ma G, Gu H, Yang Z, Cheng H (2015) A new lithium-ion battery: CuO nanorod array anode versus spinel $LiNi_{0.5}Mn_{1.5}O_4$ cathode. J Power Sources 273:561–565
[17] Jose AS, Gangaja B, Nair S, Santhanagopalan D (2019) Influence of cobalt concentration on CuO nanoplates morphology and its superior performance as Li – ion battery anode in fl uence of cobalt concentration on CuO nanoplates morphology and its superior performance as Li – ion battery anode. Mater Res Express 6:125543
[18] Ali K, Sajid M, Bakar SA, Younus A, Ali H, Rashid MZ (2024) Synthesis of copper oxide (CuO) via coprecipitation method: tailoring structural and optical properties of CuO nanoparticles for optoelectronic device applications. Hybrid Advances 6:100250
[19] Chauhan A, Verma R, Batoo KM, Kumari S, Kalia R, Kumar R, Hadi M, Raslan EH, Ahamad I (2021) Structural and optical properties of copper oxide nanoparticles: a study of variation in structure and antibiotic activity. J Mater Res 36:1496–1509
[20] Feng L, Xuan Z, Bai Y, Zhao H, Li L, Chen Y, Yang X, Su C, Guo J, Chen X (2014) Preparation of octahedral CuO micro/nanocrystals and electrochemical performance as anode for lithium-ion battery. J Alloys Compd 600:162–167
[21] Xiang JY, Tu JP, Zhang L, Zhou Y, Wang XL, Shi SJ (2010) Self-assembled synthesis of hierarchical nanostructured CuO with various morphologies and their application as anodes for lithium ion batteries. J Power Sources 195:313–319
[22] Hu L, Yang Z, Li H, Yang X, Li J, Wang P, Jin C, Zhang C (2021) Three-dimensional clusters of peony-shaped CuO nanosheets as a high-rate anode for Li-ion batteries. RSC Adv 11:10760–10766
[23] Wang C, Higgins D, Wang F, Li D, Liu R, Xia G, Lia N, Li Q, Xu H, Wu G (2014) Controlled synthesis of micro / nanostructured CuO anodes for lithium-ion batteries. Nano Energy 9:334–344
[24] Kundu M, Karunakaran G, Kolesnikov E, Gorshenkov MV, Kuznetsov D (2017) J Clust Sci 28:1595–1604
[25] Pan Q, Huang K, Ni S, Yang F, Lin S, He D (2009) Synthesis of sheaf-like CuO from aqueous solution and their application in lithium-ion batteries. J Alloys Compd 484:322–326
[26] Wang C, Higgins D, Wang F, Li D, Liu R, Xia G, Ning L, Li Q, Xu H, Wu G (2014) Controlled synthesis of micro / nanostructured CuO anodes for lithium-ion batteries. Nano Energy 9:334–344
[27] Shi L, Fan C, Sun C, Ren Z, Fu X, Qian G, Wang Z (2015) Synthesis of different CuO nanostructures from Cu(OH)2 nanorods through changing drying medium for lithium-ion battery anodes. RSC Adv 5:28611–28618
[28] Waser O, Hess M, Güntner A, Novák P, Pratsinis SE (2013) Size controlled CuO nanoparticles for Li-ion batteries. J Power Sources 241:415–422
[29] Fernando WTRS, Amaraweera THNG, Jayathilaka KMDC, Kumara LSR, Seo O, Osaka K, Sakata O, Wijesundera RP, Wijayasinghe HWMAC (2025) Facile synthesis of sponge-like microstructured CuO anode material for rechargeable lithium-ion batteries. Coatings 15:467
[30] Ren X, Liu J, Zhang W (2012) Strain effect on the electrochemical properties of Li2MnO3 cathode material: a first-principles calculation. Key Eng Mater 519:147–151
[31] Yue J, Badaczewski FM, Voepel P, Leichtwei T, Mollenhauer D, Zeier WG, Smarsly BM (2018) Critical role of the crystallite size in nanostructured $Li_4Ti_5O_{12}$ anodes for lithium-ion batteries. ACS Appl Mater Interfaces 10:22580–22590
[32] Zhang L, Feng Q, Nie A, Liu J, Wang H, Fang Y (2014) In situ study of thermal stability of copper oxide nanowires at anaerobic environment. Journal of Nano materials 1–6.
[33] Luo Z, Fu L, Zhu J, Yang W, Li D, Zhou L (2020) Cu_2O as a promising cathode with high specific capacity for thermal battery. J Power Sources 448:227569
[34] Wu Y, Wang S, Li H, Chen L, Wu F (2021) Progress in thermal stability of all-solid-state-Li-ion-batteries. Info Mat 3:827–853
[35] Ranganath SB, Hassan AS, Ramachandran BR, Wick CD (2016) Role of metal-lithium oxide interfaces in the extra lithium capacity of metal oxide lithium-ion battery anode materials. J Electrochem Soc 163:A2172–A2217
[36] Wang B, Wu XL, Shu CY, Guo YG, Wang CR (2010) Synthesis of CuO/graphene nanocomposite as a high-performance anode material for lithium-ion batteries. J Mater Chem 20:10661–10664
[37] Ferrara C, Gentile A, Marchionna S, Quinzeni I, Fracchia M, Ghigna P, Pollastri S, Ritter C, Vanacore GM, Ruffo R (2021) The missing piece: the structure of the $Ti_3C_2T_x$MXene and its behavior as negative electrode in sodium ion batteries. Nano Lett 21:8290–8297

[38] Kozawa T (2019) Lattice deformation of $LiNi_{0.5}Mn_{1.5}O_4$ spinel cathode for Li-ion batteries by ball milling. J Power Sources 419:52–57
[39] Meng J, Guo H, Niu C, Zhao Y, Xu L, Li Q, Mai L (2017) Advances in structure and property optimizations of battery electrode materials. Joule 1:522–547
[40] Xu GL, Liu X, Zhou X, Zhao C, Hwang I, Daali A, Yang Z, Ren Y, Sun CJ, Chen Z, Liu Y, Amine K (2022) Native lattice strain induced structural earthquake in sodium layered oxide cathodes. Nat Commun 13:1–12
[41] Khalate SA, Kate RS, Kim JH, Pawar SM, Deokate RJ (2017) Effect of deposition temperature on the properties of Cu_2ZnSnS_4 (CZTS) thin films. Superlattices Microstruct 103:335–342
[42] nanoparticles synthesized by microwave irradiation method. Applied Surface Science. 449: 132–143.
[43] Bindu P, Thomas S (2014) Estimation of lattice strain in ZnO nanoparticles: X-ray peak profile analysis. J Theor Appl Phys 8:123–134
[44] Abusnina MM (2016) Synthesis and characterization of kesterite Cu_2ZnSnS_4 (CZTS) thin film for solar cell application. Electronic theses and dissertations 4:203
[45] Zak AK, Majid WHA, Abrishami ME, Yousefi R (2011) X-ray analysis of ZnO nanoparticles by Williamson-Hall and size-strain plot methods. Solid State Sci 13:251–256
[46] Gibson N, Holzwarth U (2011) The Scherrer equation versus the 'Debye-Scherrer equation. Nat Nanotechnol 6:534
[47] Mishra SK, Roy H, Lohar AK, Samanta SK, Tiwari S, Dutta K (2015) A comparative assessment of crystallite size and lattice strain in differently cast A356 aluminium alloy. IOP Conf Ser Mater Sci Eng 75:6–12
[48] Saleem M, Fang RHB, Wu F, Huang QL, Xu CL, Kong CY (2012) Effect of zinc acetate concentration on the structural and optical properties of ZnO thin films deposited by sol-gel method. Intl J Phy Sci 7:2971–2979
[49] Huie MM, Bock DC, Bruck AM, Tallman KR, Housel LM, Wang L, Thieme J, Takeuchi ES, Marschilok AC (2019) Isothermal microcalorimetry: insight into the impact of crystallite size and agglomeration on the lithiation of magnetite, Fe_3O_4. ACS Appl Mater Interfaces 11:7074–7086
[50] Zhao M, Fu Y, Xu N, Li G, Wu M, Gao X (2014) High performance $LiMnPO_4$/C prepared by a crystallite size control method. J Mater Chem A 2:15070–15077
[51] Sen SK, Mortuza AA, Manir MS, Pervez MF, Hossain SMAI, Shah AM, Haque MAS, Matin MA, Hakim MA, Huda AU (2020) Structural and optical properties of sol-gel synthesized h-MoO_3nanorods treated by gamma radiation. Nano Express 1:020026
[52] Debbichi L, Marco DLMC, Pierson JF, Krüger P (2012) Vibrational properties of CuO and Cu_4O_3 from first-principles calculations, and raman and infrared spectroscopy. J Phys Chem C 116:10232–10237
[53] Siddiqui H, Parra MR, Haque FZ (2018) Optimization of process parameters and its effect on structure and morphology of CuO nanoparticle synthesized via the sol−gel technique. J Sol-Gel Sci Technol 87:125–135
[54] Wu MS, Chiang PCJ, Lin JC, Jan YS (2003) Correlation between electrochemical characteristics and thermal stability of advanced lithium-ion batteries in abuse tests short-circuit tests. Electrochim Acta 49:1803–1812
[55] Allcorn E, Kim SO, Manthiram A (2015) Thermal stability of active/inactive nanocomposite anodes based on Cu_2Sb in lithium-ion batteries. J Power Sources 299:501–508
[56] Martin L, Martinez H, Poinot D, Pecquenard B, Le Cras F (2013) Comprehensive X-ray photoelectron spectroscopy study of the conversion reaction mechanism of CuO in lithiated thin film electrodes. J Phys Chem C 117:4421–4430
[57] Jana S, Das S, Das NS, Chattopadhyay KK (2010) CuO nanostructures on copper foil by a simple wet chemical route at room temperature. Mater Res Bull 45:693–698
[58] Wang C, Li Q, Wang F, Xia G, Liu R, Li D, Li N, Spendelow JS, Wu G (2014) Morphology-dependent performance of CuO anodes via facile and controllable synthesis for lithium-ion batteries. ACS Appl Mater Interfaces 6:1243–1250
[59] Tsai SH, Tsou YL, Yang CW, Chen TY, Lee CY (2020) Applications of different nano-sized conductive materials in high energy density pouch type lithium ion batteries. Electrochim Acta 362:137166
[60] Kundu M, Karunakaran G, Kolesnikov E, Gorshenkov MV, Kuznetsov D (2017) Negative Electrode Comprised of Nanostructured CuO for Advanced Lithium Ion Batteries. J Clust Sci 28:1595–1604
[61] Lee J, Choi S, Park S (2013) A simple fabrication of interconnected CuO nanotube electrodes for high- performance lithium-ion batteries. Chem Asian J 00:0–0
[62] Seo SD, Jin YH, Lee SH, Shim HW, Kim DW (2011) Low-temperature synthesis of CuO-interlaced nanodiscs for lithium ion battery electrodes. Nanoscale Res Lett 6:1–7
[63] Mohapatra S, Nair SV, Santhanagopalan D, Rai AK (2016) Nanoplate and mulberry-like porous shape of CuO as anode materials for secondary lithium ion battery. Electrochim Acta 206:217–225
[64] Wan M, Jin D, Feng R, Si L, Gao M, Yue L (2011) Pillow-shaped porous CuO as anode material for lithium-ion batteries. Inorg Chem Commun 14:38–41

Terms and Conditions

Springer Nature journal content, brought to you courtesy of Springer Nature Customer Service Center GmbH (“Springer Nature”).
Springer Nature supports a reasonable amount of sharing of research papers by authors, subscribers and authorised users (“Users”), for small-scale personal, non-commercial use provided that all copyright, trade and service marks and other proprietary notices are maintained. By accessing, sharing, receiving or otherwise using the Springer Nature journal content you agree to these terms of use (“Terms”). For these purposes, Springer Nature considers academic use (by researchers and students) to be non-commercial.
These Terms are supplementary and will apply in addition to any applicable website terms and conditions, a relevant site licence or a personal subscription. These Terms will prevail over any conflict or ambiguity with regards to the relevant terms, a site licence or a personal subscription (to the extent of the conflict or ambiguity only). For Creative Commons-licensed articles, the terms of the Creative Commons license used will apply.
We collect and use personal data to provide access to the Springer Nature journal content. We may also use these personal data internally within ResearchGate and Springer Nature and as agreed share it, in an anonymised way, for purposes of tracking, analysis and reporting. We will not otherwise disclose your personal data outside the ResearchGate or the Springer Nature group of companies unless we have your permission as detailed in the Privacy Policy.
While Users may use the Springer Nature journal content for small scale, personal non-commercial use, it is important to note that Users may not:

1. use such content for the purpose of providing other users with access on a regular or large scale basis or as a means to circumvent access control;
2. use such content where to do so would be considered a criminal or statutory offence in any jurisdiction, or gives rise to civil liability, or is otherwise unlawful;
3. falsely or misleadingly imply or suggest endorsement, approval , sponsorship, or association unless explicitly agreed to by Springer Nature in writing;
4. use bots or other automated methods to access the content or redirect messages
5. override any security feature or exclusionary protocol; or
6. share the content in order to create substitute for Springer Nature products or services or a systematic database of Springer Nature journal content.

In line with the restriction against commercial use, Springer Nature does not permit the creation of a product or service that creates revenue, royalties, rent or income from our content or its inclusion as part of a paid for service or for other commercial gain. Springer Nature journal content cannot be used for inter-library loans and librarians may not upload Springer Nature journal content on a large scale into their, or any other, institutional repository.
These terms of use are reviewed regularly and may be amended at any time. Springer Nature is not obligated to publish any information or content on this website and may remove it or features or functionality at our sole discretion, at any time with or without notice. Springer Nature may revoke this licence to you at any time and remove access to any copies of the Springer Nature journal content which have been saved.
To the fullest extent permitted by law, Springer Nature makes no warranties, representations or guarantees to Users, either express or implied with respect to the Springer nature journal content and all parties disclaim and waive any implied warranties or warranties imposed by law, including merchantability or fitness for any particular purpose.
Please note that these rights do not automatically extend to content, data or other material published by Springer Nature that may be licensed from third parties.
If you would like to use or distribute our Springer Nature journal content to a wider audience or on a regular basis or in any other manner not expressly permitted by these Terms, please contact Springer Nature at

onlineservice@springernature.com